レーザセンシング学会誌　5巻1号　令和6年4月15日発行

ISSN 2435-6239

JOURNAL OF LASER RADAR SOCIETY OF JAPAN

レーザセンシング学会誌

2024
Vol.5 No.1

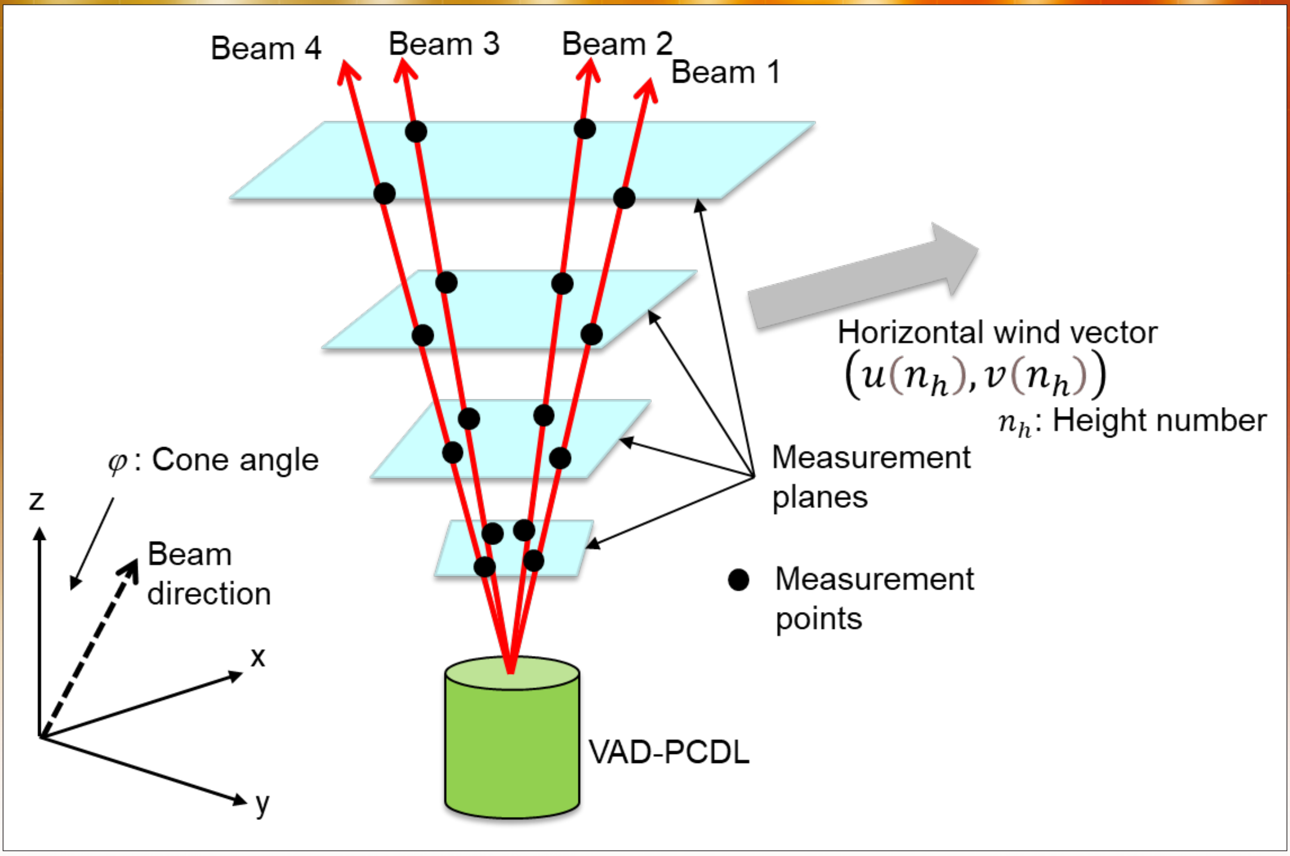

13ページの論文参照

レーザセンシング学会
Laser Radar Society of Japan
https://www.laser-sensing.jp/

LRSJ
Laser Radar Society of Japan　レーザセンシング学会

レーザセンシング学会誌

Journal of Laser Radar Society of Japan

Volume 5, Number 1（April 2024）

◆巻頭言

Prefatory note

「下流側」からライダー研究を考える

Lidar research from the viewpoint of a downstream researcher

甲斐憲次 Kenji Kai ………………………………………… 1

◆論文

Paper

Decadal (2011–2020) stratospheric aerosol variability observed by lidar over Saga, Japan

Osamu Uchino, Tetsu Sakai, Isamu Morino, Tomohiro Nagai, Hiroshi Okumura, Yoshitaka Jin, Atsushi Ugajin, Tomoaki Nishizawa, Atsushi Shimizu, Tsuneo Matsunaga, and Kohei Arai ………… 4

Full-parameter performance simulation theory for velocity azimuth display pulsed coherent Doppler lidar, and error analysis on wind speed measurement in shear flow

Shumpei Kameyama ………………………………………… 13

◆ニュース

第 41 回レーザセンシングシンポジウム開催報告

酒井 哲，染川智弘，吉田 智，西橋政秀，及川栄治，永井智広，瀬古 弘 ……………………… 29

AGU Fall Meeting 2023 参加報告

ラゴロサス ノフェル（Nofel Lagrosas）………………………………………… 33

◆学会だより ………………………………………… 34

- 学会誌への投稿案内
- 「学位論文紹介」投稿のお願い

正誤表 …… 35

編集後記 …… 36

巻頭言

LRSJ
Laser Radar Society of Japan　レーザセンシング学会

レーザセンシング学会誌　第5巻第1号(2024)

「下流側」からライダー研究を考える

甲斐 憲次

名古屋大学名誉教授，名古屋大学大学院環境学研究科（〒464–8601 名古屋市千種区不老町）

Lidar research from the viewpoint of a downstream researcher

Kenji Kai

Graduate School of Environmental Studies, Nagoya University,
Furo-cho, Chikusa-ku, Nagoya 464–8601

（Received February 13, 2024）

I review the lidar research from the view point of a downstream researcher.

キーワード：ライダー研究，国際レーザーレーダー会議，レーザセンシングシンポジウム
Key Words: Lidar research, International Laser Radar Conference, Laser Sensing Symposium

私は，学位取得後，気象庁（5年），筑波大学（12年），名古屋大学（21年），茨城大学（3年）で気象と大気環境の教育・研究・行政に携わってきた．40年間，いつもライダー研究との関りがあった[1)]．ライダー研究は，ライダーそのものを開発する「上流側」の研究と，ライダーから得られるデータを利用する「下流側」の研究に分けることができる．私は下流側の研究者の立場から，いままで関わってきたライダー研究を述べたい．

私は大学院の頃（1970年代後半），大気乱流の研究に没頭していた．超音波風速温度計を用いて大気中の乱流を観測し，ひたすらスペクトル解析をした．まったくでたらめに見える乱流も，そのスペクトルの高周波側はコロモゴルフの-5/3則に従う．この法則（局所等方性乱流）が乱流解析の基準となる．乱流研究者は，だれもがこの美しい法則に心を動かされる．私は研究の世界に入り，1981年理学博士を取得した．

筑波大学に3年勤務した後，1984年，気象庁観測部産業気象課に出向した．所掌業務は，国内外の農業気象災害の監視である．係長と二人で，世界の主要農産地，すなわち南北アメリカ・オーストラリア・アジア・ソ連・アフリカおよび日本の気候データを分析し，農業気象災害を調べた．気象庁のルーチン業務にも慣れた．研究職に興味があるものの，チームワークでやる仕事の面白さも感じ始めていた．

本庁勤務2年目のある日，気象研究所気象衛星観測研究部の部長さんから電話があり，「気象研究所でライダーの研究をやりませんか」とお誘いをいただいた．「ライダーは何かわかりませんが，私の研究歴でライダー研究ができるならば，ぜひ，筑波の研究所に移りたいです」と私は二つ返事で快諾した．部長さんは，「甲斐さんはまだ若いので（当時33歳），ライダー研究への転向は大丈夫ですよ．本格的な研究は，内野修さんがNASAラングレー研究所から帰国する1年後になります」との言葉を頂いた．

1986年4月，筑波の気象研究所に転勤した．これが私のライダーとの関りの始まりだ．内野さんが帰国するまでの1年間は，大学院時代に戻ったように，ライダー関連分野の勉強をした．具体的な研究業務はなく，ひたすら勉強する毎日だった．勉強ばかりしていて，給料がいただけるのは，不思議な気がした．

一方，隣の国立環境研究所では，竹内延夫・清水浩・笹野泰弘・杉本伸夫・松井一郎・林田佐智子ら（敬称略）一流の研究者を中心に，ライダー研究グループが形成されつつあった．当時は，大気汚染の深刻化を背景に，レーザー技術を用いた大気汚染物質の遠隔計測法を開発するという夢があった．バブル前の好景気に沸き，筑波研究学園都市の研究機関にも潤沢な研究資金があった．国研や大学で大型ライダーの開発計画

が持ち上がると，日本を代表する大企業（東芝，日立，NEC，IHIなど）が入札に参加していた．バブル期以降は，潮が引くように，多くの企業がライダー開発から撤退した．ライダー装置は研究用が主で，多くの需要が見込めなかったのだろう．結局のところ，製品化され普及した大気計測ライダーは，空港に設置されているドップラーライダーと雲底計（シーロメーター）であろうか．このほか，NASAとシグマスペース社が共同で開発したマイクロパルスライダーや，最近製品化されたヴァイサラ社の水蒸気ライダーなどがある．

1987年，NASAラングレー研究所から内野さんが戻り，本格的なライダー研究が始まった．すでにルビーライダーのデータが蓄積されていたので，3名の研究員でそれぞれ成層圏エアロゾル，雲，黄砂の研究が始まった．私は黄砂を担当した1)．翌年，オゾンライダーの大型予算がつき，本格的なライダー研究が始まった．

内野さんのアドバイスを受けながら，ライダーデータの解析プログラムを作り作図した．空がきれいな冬の晴天日のデータは，散乱比が上空できれいな高度分布（レイリー散乱）をする．レッドペーパーで海外の火山噴火が報告されると，成層圏にスパイク状のピークが現れる．データの時系列をじっくりみると，火山灰がゆっくりと拡散しながら重力落下する様子が見える．面白さを感じた．レイリー散乱のプロファイルと比較することにより，ライダーの散乱データが基準化される．それは，若い頃みたコロモゴルフの-5/3則のような感じがした（個人的な印象である）．

1988年の始め，私はAMSの雑誌で，第14回国際レーザーレーダー会議（ILRC14）がイタリアで開催されることを知った．旅費の目途は立たなかったが，私と内野さんはとにかく，私費でILRC14に参加することを決めた．初めての海外旅行である．海外で英語が通じるだろうかとの不安が付きまとった．十分な旅費がなかったので，イタリアへの旅行は，格安航空（当時）のシンガポール航空を利用して，南回りでイタリアに向かった．なんと23時間もかかった．最初の英語ショックは，機内であった．スチュワーデスにコーヒーを注文すると，なんと紅茶が出てきた．Coffeeの発音は意外と難しい．英語では，「**カ**フィー」と発音しなければならない．騒音のある機内で日本式に単調に「コーヒー」と発音すると，通じなかった．

国際レーザーレーダー会議（ILRC14）は，1988年6月20–24日，美しい北イタリアのリゾートInnichen-San Candidoで開催された．ILRC14では，国際会議の楽しさを味わうことができた．参加者は，最先端の研究をしていると言う高揚感があった．最新の研究成果を聞くのは楽しかった．世界の各国にこれほど多くの研究者がライダー研究をしているのか．現地では，日本人研究者の団結力を感じた．私は準備した英語を話したが，相手の質問がよく分からないことが多かった．そんな時，小林喬郎先生が助っ人に入られ，何度も救われた．夕方からワインを飲みながら，ポスターセッションが始まった．アルコールのおかげで，質問と応答は比較的滑らかだった．こんな粋なやり方があるものかと感心した．1970年代，イタリア経済の落ち込みが盛んに日本でも報道されていたが，リゾート施設の豊かさは日本とは比較ならないくらい良かった．6月は天候もよく，June Brideの意味がよく分かった．アルプスのふもとにある美しいリゾートにいると，研究の感覚が研ぎ澄まされるように感じた．

私の発表は，なんと最終日6月24日の最終発表であった．毎晩ホテルで練習したお陰で，発表原稿を丸暗記できた．恥ずかしながら，この最初の国際会議での発表が，私の研究歴の中で最も良かったように思う．黄砂の発生と輸送に関して，アメリカ，ドイツ，ロシアなどの研究者と話をすることができたのは幸いであった．研究費があり，研究成果があがっているときは，万難を排して参加すべきシンポジウムの一つだと思う．

国際レーザーレーダー会議（ILRC14）が豊かなのは，NASAの強力なサポートがあるように感じた．参加者は，新しいことに挑戦するNASAの姿，そして潤沢な資金にひかれたと思う．NASAは，将来のスペースライダー計画に向け，研究のすそ野を拡げる活動にも注力していた．CALIPSOが成功したのはいくつの奇跡が連続したことにあるが（A.H. Omar氏の私信），技術的な成功のほか，ソフト的な成功があげられる．その一つがデータを適切に公開して，研究のすそ野を拡げたことだろう．スペースライダーの開発という「上流側」の研究ほか，ライダーデータの利用という「下流側」の研究にも十分な予算が用意されていた．その結果，CALIPSOデータを利用する研究コミュニティが形成された．ライダーデータの利用という視点は，日本と欧州が協力して開発を進める地球観測衛星EarthCARE（Earth Cloud Aerosol and Radiation Explorer）でも極めて重要である2)．

このように，国際レーザーレーダー会議（ILRC14）は，私がライダー研究を続ける切っ掛けとなった．もう一つは，レーザセンシングシンポジウム（LSS）である．LSSは，日本版ILRCとも言える．異分野の企業，国立研究機関，大学の研究者が一堂に会する，コンパクトな集まりである．LSSは最初の頃，温泉で開催された．昼間の研究会の後は，「古き良き」大宴会が行われた．私は，「LSSは温泉で開催すべきである」との考えである（個人的な見解である）．昼間の研究会では聞けなかったことが，宴会場で聞けることがある．論文で名前だけ知っている研究者とじかに話をすると，論文のポイントがよく分かる．また，研究の姿勢やポリシーなども伺うことができる．共同研究には必須の情報である．

国際サッカー連盟FIFAは，4年に一度，ワールドカップを主催する．1年に一度，レーザセンシングシンポジウムを主催するレーザセンシング学会（LRSJ）は，FIFAと似ているなと思うことがある．経験則であるが，100人くらいの規模だと研究者の顔と名前が一致し，また方向性も一致して，学会活動がアクティブになる．LRSJはいま曲がり角を迎えているように思う．LRSJは，本格的な学会を目指すのか，あるいはFIFAのように，1年1回のシンポジウムを開催する研究会として存続するか．現在，LRSJはニューズレター，電子ジャーナルなどを発行し，学会の形式を整えつつある．

私がベースとする学会は気象学会で，そのほか，地理学会，沙漠学会，エアロゾル学会なども所属している．伝統のある学会はそれなりの良さがあるが，参加者が固定化して，伝統ゆえ大胆な取組みは難しい感じがする．一方，レーザセンシング学会（LRSJ）は，常に異分野との交流があり，新しい装置や手法の情報が得られる．また，国際レーザーレーダー会議（ILRC）の遺伝子ともいえる明るさと国際性・先進性がLRSJにもある．このようなメリットを生かしつつ，LRSJがますます発展することを祈念する．

引用文献

1）甲斐憲次，“アジアダストのライダー観測，”レーザセンシング学会誌，**1**（1），29–42（2020）．
2）杉本伸夫，“巻頭言　ライダー観測とデータ利用，”レーザセンシング学会誌，**4**（1），2–4（2023）．

Paper

LRSJ
Laser Radar Society of Japan レーザセンシング学会

Journal of Laser Radar Society of Japan, Vol. 5, No. 1(2024)

Decadal (2011–2020) stratospheric aerosol variability observed by lidar over Saga, Japan

Osamu Uchino*[1, 2], Tetsu Sakai[1], Isamu Morino[2], Tomohiro Nagai[1],
Hiroshi Okumura[3], Yoshitaka Jin[2], Atsushi Ugajin[2], Tomoaki Nishizawa[2],
Atsushi Shimizu[2], Tsuneo Matsunaga[2], and Kohei Arai[3]

[1]*Meteorological Research Institute, 1−1 Nagamine, Tsukuba, Ibaraki 305−0052, Japan*
[2]*National Institute for Environmental Studies, 16−2 Onogawa, Tsukuba, Ibaraki 305−8506, Japan*
[3]*Saga University, 1 Honjou, Saga, Saga 840−8502, Japan*

(Received July 20, 2023; revised October 2, 2023; accepted October 11, 2023)

Lidar observations at the wavelength of 532 nm during 2011−2020 in Saga, Japan, revealed that stratospheric aerosols increased after the eruptions of Nabro volcano in Eritrea on 12 June 2011 and Raikoke volcano in the central Kuril Islands on 22 June 2019. Maximum values of the backscattering ratio and the integrated backscattering coefficient of stratospheric aerosols from tropopause altitude to 33 km after the Nabro eruption were 3.70 at 18.22 km on 23 June 2011 and 3.65×10^{-4} sr^{-1} on 25 July 2011, respectively; those after the Raikoke eruption were 1.89 at 17.47 km on 8 August 2019 and 3.01×10^{-4} sr^{-1} on 1 November 2019, respectively. Assuming a lidar ratio of 50 sr at 532 nm, the maximum stratospheric aerosol optical depth over Saga during the ten-year period from 2011 to 2020 was estimated to be 0.018 on 25 July 2011.

Stratospheric smoke particles from the Canadian forest fires in August 2017 were also detected. The degree of depolarization of smoke particles was about 0.1−0.18, and this value persisted for a long period of time, from 31 August 2017 to 22 February 22, 2018. These lidar data are useful for investigating the effects of stratospheric aerosols on climate and the ozone layer.

Key Words: Lidar, Stratospheric Aerosol, Volcanic eruption, Smoke

1. Introduction

Monitoring of the stratospheric aerosol layer is important because stratospheric aerosols affect the climate through radiative processes and the ozone layer through heterogeneous chemical reactions at the aerosol surface.[1, 2)] In addition, it is useful to investigate the stratospheric aerosols in the column-averaged dry air mole fractions of CO_2 and CH_4 (XCO_2 and XCH_4), products of the Greenhouse gases Observing SATellite (GOSAT).[3)] As stratospheric aerosols with an optical thickness of 0.01 have been found to have an effect on XCO_2 at high latitudes in the Southern Hemisphere winter derived from the Orbiting Carbon Observatory-2 (OCO-2) satellite, a Gaussian stratospheric aerosol profile was introduced to improve the retrieval algorithm of OCO-2.[4)]

In 2008, the National Institute for Environmental Studies (NIES), Japan, in cooperation with the Meteorological Research Institute, Japan, developed a Mie-scattering lidar system to evaluate the influence of tropospheric and stratospheric aerosols and clouds on the GOSAT product with Total Carbon Column Observing Network Fourier Transform Spectrometer (TCCON FTS) and skyradiometer.[3)] The Mie-scattering lidar system uses two wavelengths of the Nd:YAG laser (1064 nm and 532 nm) and can also observe the depolarization ratio at 532 nm. Using this lidar, we observed an increase in stratospheric aerosols caused by the Mt. Sarychev (48.08°N, 153.23°E) volcanic eruption on 12 June 2009.[5)] To validate the tropospheric ozone data derived from the GOSAT thermal infrared spectra, a tropospheric ozone differential absorption lidar (DIAL) system was developed at NIES from 2009 to 2010 and installed on a container together with the Mie-scattering lidar. In March 2011, the container containing the lidar systems was moved from NIES in Tsukuba to Saga University, Japan (33.24°N, 130.29°E), about 950 km to the southwest, after which we started lidar observations. We have previously reported several observation and analysis results obtained using the Mie-scattering lidar and the ozone DIAL, 5, 6) and here we report on the stratospheric aerosol layer variations during 2011–2020 observed using the Mie-scattering lidar. First, the lidar system and data analysis method are described; next, the lidar observation results of stratospheric aerosols for 2011–2020 are presented; finally, the negative radiative forcing due to the increase in stratospheric aerosols after the 2011 Nabro and 2019 Raikoke volcanic eruptions is discussed.

2. Lidar system and data analysis

The laser output energy used to observe stratospheric aerosols at a wavelength of 532 nm was 130 mJ per pulse with a repetition rate of 10 Hz. The transmitted laser beam divergence was 0.2 mrad using a beam expander with a magnification factor of 5. The receiving telescope was a Schmidt-Cassegrain type with an aperture of 30.5 cm and a receiving field of view of 1.0 mrad. Three photomultiplier tubes (PMTs, R3234–01) were used as detectors, two to detect the parallel (P) component of the same polarization as the laser and one for the perpendicular (S) component. For signal processing, a 12-bit AD conversion and photon counting system (TR 20–160)was used.5)

The backscattering ratio (BSR) is defined as

$$BSR = \frac{BR + BA}{BR}, \qquad (1)$$

where BR and BA are the molecular and particle backscattering coefficients, respectively. Previously, radiosonde data at Fukuoka were used to calculate BR, but since radiosondes sometimes do not reach more than 30 km, JRA-55 reanalysis data7) were used instead to calculate BR and tropopause altitude. Because the wavelength of 532 nm is subject to ozone absorption, monthly average values for Kagoshima (31.55°N, 130.55°E) were used as the ozone model.8) The lidar ratio S (the ratio of particle extinction to backscattering coefficient) was assumed to be 50 sr in this analysis.9) The lidar backscatter signal was normalized to $BSR = 1.02$ (i.e., aerosol backscattering coefficient (BA) is 2% of the molecular backscattering coefficient (BR)) at 32–37 km altitude based on studies using satellite-borne stratospheric aerosol measurements.10–12) We derived backscattering ratio profiles with an inversion method.13) The vertical and time resolution of the raw lidar data were 7.5 m and 1 min, respectively. To improve the signal-to-noise ratio, lidar data were accumulated over an altitude of 150 m and temporally overnight. The time accumulation depended on the season because the sunrise and sunset were different depending on the season.

We obtained the integrated backscattering coefficient by summing up BA from the tropopause altitude to an altitude of 33 km. When cirrus clouds were present above the tropopause, we set the lower limit of the integration to just above the altitude of the cirrus clouds.

In this paper, the total linear depolarization ratio (TDR) is defined as

$$TDR = \frac{S}{P}, \qquad (2)$$

where P and S are the parallel and perpendicular components of the backscattered signals, respectively. The total linear depolarization ratio δ so far5) is

$$\delta = \frac{S}{P + S}. \qquad (3)$$

The relationship between TDR and δ is as follows

$$TDR = \frac{\delta}{1 - \delta}. \qquad (4)$$

Therefore, TDR is larger than δ.

The particle depolarization ratio PDR is calculated by

$$PDR = \frac{(1+TDRm)TDR \cdot BSR - (1+TDR)TDRm}{(1+TDRm)BSR - (1+TDR)}, \qquad (5)$$

where $TDRm$ is the linear depolarization ratio of air molecules.[14] We used $TDRm = 3.66 \times 10^{-3}$.[15]

3. Lidar observation results

During 2011–2020 over Saga, stratospheric aerosols increased mainly as the results of two volcanic eruptions, Nabro and Raikoke; in addition, smoke particles from large forest fires in Canada were detected in the stratosphere. In this section we discuss these lidar observational results. The lidar observation site (Saga) and the locations of the volcanoes (Nabro and Raikoke) and pyrocumulonimbuses (pyroCbs) that contributed to the increase in stratospheric aerosols are shown in Fig. 1.

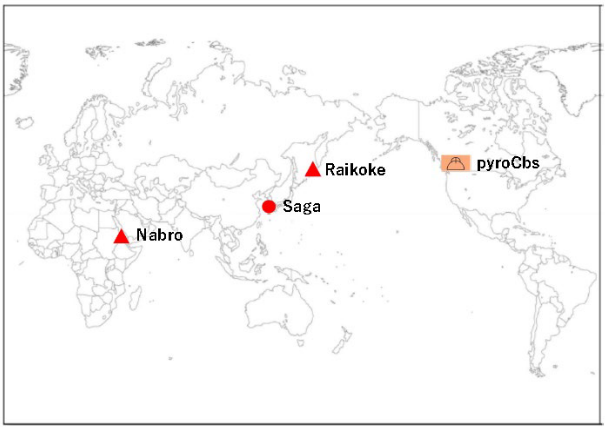

Fig. 1 Lidar observation site (Saga) and the locations of volcanoes (Nabro and Raikoke) and pyrocumulonimbuses (pyroCbs).

3.1. Stratospheric aerosol increase due to the June 2011 eruption of Nabro volcano

Nabro volcano (13.37°N, 41.70°E) in Eritrea erupted on 12 June 2011. The total mass of SO_2 produced by the eruption was estimated to be 1.5 Tg.[16] Figure 2 shows vertical profiles of the aerosol backscattering ratio (*BSR*), total depolarization ratio (*TDR*), and particle depolarization ratio (*PDR*) at 532 nm over Saga. New aerosol layers with double peaks were observed on 23 June 2011, about 11 days after the eruption. The peak values of *BSR* were 2.25 and 3.70 at altitudes of 17.17 km and 18.22 km, respectively. The values of *PDR* were 0–0.016 at 17.2–18.2 km. Aerosols were probably composed of spherical particles because *PDR* was very small; however, some non-spherical particles were seen in the lower regions of the layers on 29 August 2011, and *PDR* was 0.03 at 16.4 km. An increase in stratospheric aerosols after the 2011 Nabro eruption was also confirmed by lidar observations at Tsukuba (36.1°N, 140.1°E).[17]

3.2. Increase in stratospheric aerosols from the Raikoke volcanic eruption in June 2019

The Raikoke volcano (48.29°N, 153.25°E) in the central Kuril Islands erupted on 22 June 2019. The SO_2 injected into the upper troposphere and lower stratosphere by the Raikoke eruption was estimated to be 2.1±0.2 Tg (larger than the initial estimate of 1.5±0.2 Tg from earlier studies),[18, 19] and 40.5% (0.85 Tg) of the total SO_2 mass was injected into the lower stratosphere.[20] Following the Raikoke eruption, stratospheric aerosol optical depth (*sAOD*) values increased in the whole Northern Hemisphere.[21]

Vaughan et al.[22] detected a thin layer at an altitude of 14 km late on 3 July, with the first detection of the main aerosol cloud on 13 July by a Raman lidar system based at the Capel Dewi Atmospheric Observatory, UK (52.4°N, 4.1°W). The Mauna Loa lidar first observed a 1-km-thick aerosol layer at an altitude of 26 km on September 24 after the Raikoke eruption.[23]

At Saga, stratospheric aerosols increased on 8 August 2019 (Fig. 3). The maximum value of BSR was 1.89 at 17.47

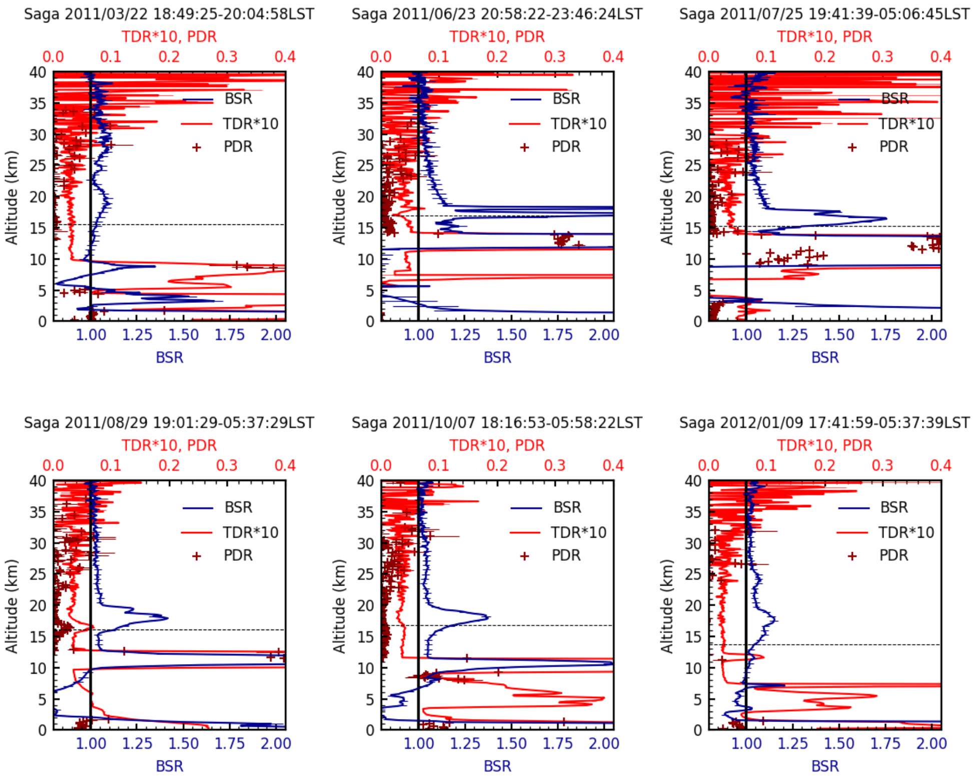

Fig. 2 Vertical profiles of aerosol backscattering ratio (*BSR*), total depolarization ratio (*TDR*), and particle depolarization ratio (*PDR*) at 532 nm over Saga, Japan, before and after the Nabro volcanic eruption in June 2011. LST stands for local standard time. The horizontal dotted lines show the mean tropopause altitudes.

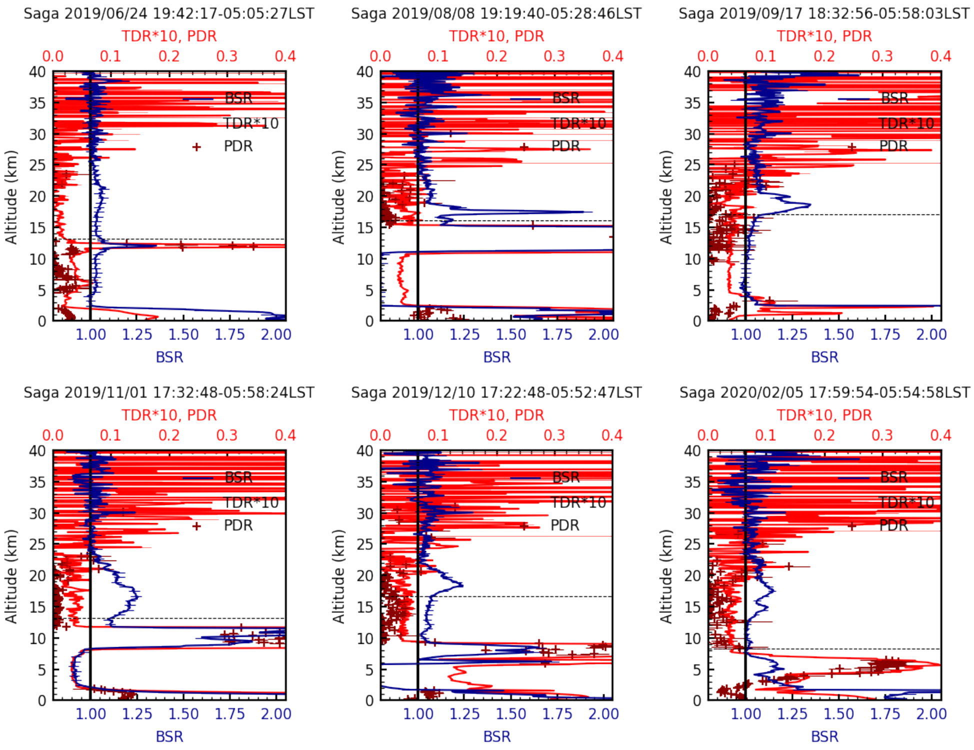

Fig. 3 Vertical profiles of aerosol backscattering ratio (*BSR*), total depolarization ratio (*TDR*), and particle depolarization ratio (*PDR*) at 532 nm over Saga, Japan, after the Raikoke volcanic eruption in June 2019. The horizontal dotted lines show the mean tropopause altitudes.

km on 8 August after the Raikoke eruption. The *BSR* peak of the background stratospheric aerosol layer composed of sulfuric acid particles mainly generated from carbonyl sulfide (COS) originating in the troposphere is around 20 km as shown on 24 June 2019. The *BSR* peak due to volcanic eruptions is approximately determined by the SO_2 injection altitude, i.e., the height of potential temperature. From September 2019 to February 2020, the *BSR* peak of the stratospheric aerosol layer was located around 18 km. Because the *PDR* was small, the particles were inferred to be sulfuric acid particles produced by chemical reaction of SO_2.

The Ulawun volcano in Papua New Guinea (5.05°S, 151.33°E) erupted on 26 June and 3 August 2019. The total mass of SO_2 from the two explosions was estimated to be 0.3 Tg. The Ulawun plume was transported mainly towards the south. Possible transport towards the north within the Brewer-Dobson Circulation was masked by already increased *sAOD* values from the Raikoke eruption in the Northern Hemisphere.[21] Lidar observations at Saga also did not clearly capture the impact of the Ulawun volcanic eruption.

3.3. Detection of smoke particles from large Canadian forest fires in summer 2017

Pyrocumulonimbus (pyroCb) from large forest fires can inject material containing smoke particles into the lower stratosphere, similar to volcanic explosions.[24] The mass of smoke aerosol particles injected into the lower stratosphere from five near-simultaneous intense pyroCbs occurring in western North America on 12 August 2017 was comparable to that of a moderate volcanic eruption and an order of magnitude larger than previous benchmarks for extreme pyroCb activity.[25]

Extreme levels of Canadian wildfire smoke were observed in the stratosphere over central Europe on 21–22 August 2017 by European Aerosol Research Lidar Network (EARLINET) lidars.[26] The smoke plume was also detected by lidar at Observatoire de Haute-Provence (43.9°N, 5.7°E) in France on 24 August as a 1-km-thick layer centered at 14.9 km; the peak *BSR* values were 8–10 around 19 km on 29 August.[27] The first smoke layer was observed between 15.0 km and 15.8 km with the maximum *BSR* of 5.8 at 15.4 km over Tomsk (56.48°N, 85.05°E) in Russia on 26 August 2017.[28]

On 31 August 2017, an aerosol layer containing smoke particles with peak values of 2.0 for *BSR*, 0.08 for *TDR*, and 0.17 for *PDR* was observed at an altitude of 17.62 km over Saga (Fig. 4). The smoke layer rose to 20.31 km on 9 Octo-

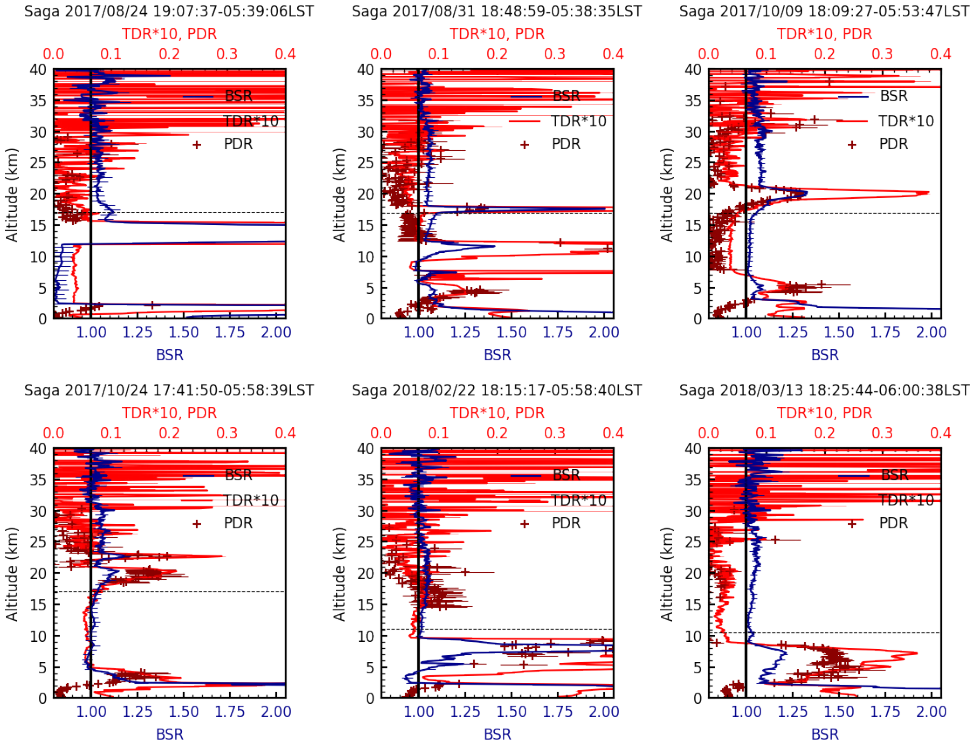

Fig. 4 Vertical profiles of aerosol backscattering ratio (*BSR*), total depolarization ratio (*TDR*), and particle depolarization ratio (*PDR*) at 532 nm over Saga, Japan, after Canadian forest fires in August 2017. The horizontal dotted lines show the mean tropopause altitudes.

ber 2017. Furthermore, on October 24, in addition to the layer near 20.31 km, a layer with a large *PDR* value was detected at 22.71 km. The smoke layer rose owing to solar heating of black carbon.[29] High values of *PDR* (>0.1) were observed at an altitude of 16–20 km until February 2018.

A high particle depolarization ratio of 0.18 in a stratospheric layer from 15–16 km altitude and a small particle depolarization of 0.03 in a tropospheric layer at 5–6.5 km were observed at 532 nm by the Leipzig (51.3°N, 12.4°E) lidar system in Germany on 22 August 2017.[30] A smoke *PDR* of 0.18–0.20 was observed at Lille (50.61°N, 3.14°E) in France in late August 2017.[31] These large *PDR* values would be expected to persist in the stratosphere because there is less water vapor in the stratosphere. Subsequently, smoke particles or aerosols mixed with smoke particles might have been transported to the troposphere in March 2018, because *PDR* values were small at ca. 20 km altitude on 13 March 2018 (Fig. 4).

4. Integrated backscattering coefficients of stratospheric aerosols

The temporal variation of the integrated backscattering coefficient (*IBC*) from tropopause to an altitude of 33 km and the tropopause altitude over Saga are shown in Fig. 5. In general, the tropopause altitude was low in winter to spring and high in summer. After the 2011 Nabro eruption and the 2019 Raikoke eruption, the IBC values clearly increased. The maximum *IBC* after the Nabro eruption was 3.65×10^{-4} sr^{-1} on 25 July 2011, and the maximum *IBC* after the Raikoke eruption was 3.01×10^{-4} sr^{-1} on 1 November 2019.

In our previous paper,[5] the maximum value of *IBC* was 4.19×10^{-4} sr^{-1} on 23 June 2011 after the Nabro eruption, whereas in this paper it was 3.65×10^{-4} sr^{-1} on 25 July 2011. The tropopause altitude on June 23 was 16.94 km from JRA-55, but it was 15.66 km from the radiosonde data of Fukuoka, near Saga, that was used in the previous paper. Calculating the *IBC* from 15.66 km to 33 km on June 23 gives a value of 3.93×10^{-4} sr^{-1}, which might be the maximum value after the Nabro eruption. The tropopause altitude from JRA-55 data seems to be higher than that from radiosonde data. The difference between the *IBC* values of 4.19×10^{-4} sr^{-1} and 3.93×10^{-4} sr^{-1} is due to differences in normalization and integration time.

After the eruption of Kelud volcano (7.94°S, 112.31°E) on February 13, 2014, volcanic ash-containing aerosols with *BSRs* of 1.07 and 1.12 and *PDRs* of 0.05 and 0.08 were observed around 17 km altitude on April 10 and 12, respectively. The *IBC* values were 9.93×10^{-5} sr^{-1} and 1.09×10^{-4} sr^{-1}, respectively, and there was no significant increase. The impact of Ambae (15.39°S, 167.84°E) eruption in April and July 2018 could not be detected at Saga.

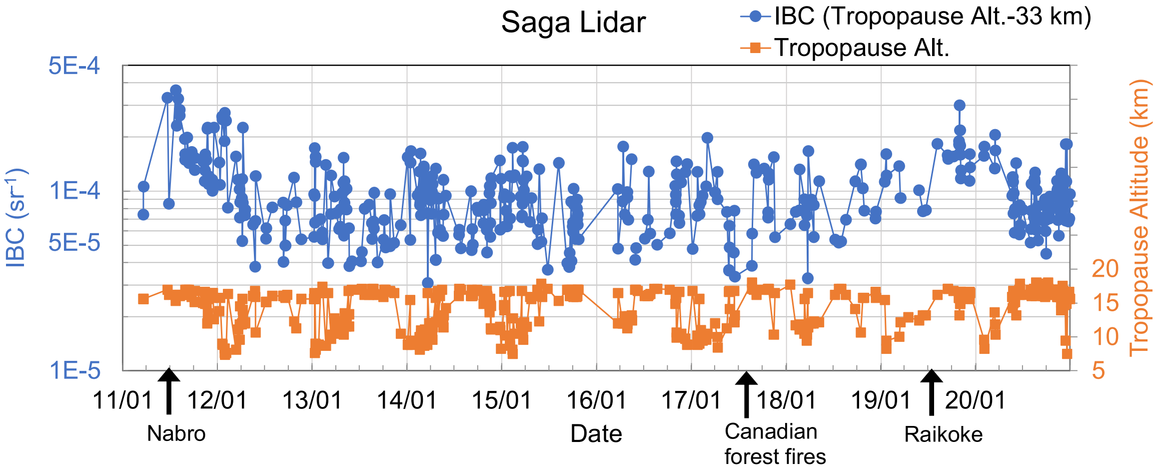

Fig. 5 Temporal variation of the integrated backscattering coefficient (*IBC*) from tropopause to an altitude of 33 km and tropopause altitude over Saga, Japan from 2011 to 2020. Arrows on the horizontal axis indicate the dates of volcanic eruptions and forest fires.

5. Discussion and concluding remarks

Lidar observations at Saga obtained over a 10-year period (2011–2020) demonstrated that stratospheric aerosols increased after the June 2011 Nabro volcanic eruption and the June 2019 Raikoke volcanic eruption. The maximum values of *BSR* and *IBC* after the Nabro eruption were 3.70 at 18.22 km altitude on 23 June 2011 and 3.65×10^{-4} sr^{-1} on 25 July 2011, respectively; those after the Raikoke eruption were 1.89 at 17.47 km on 8 August 2019 and 3.01×10^{-4} sr^{-1} on 1 November 2019, respectively. Assuming a lidar ratio of 50 sr at 532 nm, the maximum stratospheric aerosol optical depth (*sAOD*) over Saga between 2011 and 2020 was estimated to be 0.018 on 25 July 2011. This *sAOD* is one-sixteenth of the maximum *sAOD* of 0.3 observed in February 1992 by the Tsukuba lidar after the Pinatubo eruption.[32] The largest mean optical thickness of the Pinatubo-associated layer was 0.31 at 500 nm on 23 August 1991 in the latitude zone 20°S to 30°N,[33] and monthly means of *sAOD* reached 0.2 in early 1992 at three lidar stations, Naha (26.2°N, 127.7°E) and Tsukuba in Japan and Garmisch-Partenkirchen (47.5°N, 11.1°E) in Germany.[34] Although the *sAOD* of the stratospheric aerosols from the 2011 Nabro eruption was approximately 16 times smaller than the *sAOD* of the 1991 Pinatubo eruption, the resulting negative radiative forcing cannot be ignored, as discussed below.

The annual mean *IBC* value from 2013 to 2018, when stratospheric aerosols were considered normal, was 8.95×10^{-5} sr^{-1}. The annual average *IBC* in 2011 after the Nabro eruption was 1.76×10^{-4} sr^{-1}, 8.65×10^{-5} sr^{-1} higher than the annual mean. Converting these values to *sAOD* yields an increase of 0.0043. In addition, the IBC was 1.49×10^{-4} sr^{-1} in 2019 after the Raikoke eruption, 5.95×10^{-5} sr^{-1} larger than the 2013–2018 annual mean, and yielding an *sAOD* increase of 0.0030. The corresponding increases of negative radiative forcing in 2011 and 2019 were roughly 0.11 W m^{-2} and 0.07 W m^{-2}, respectively, based on a conversion factor from *sAOD* to radiative forcing of 25 W m^{-2}.[35,36] The increase in radiative forcing due to CO_2 from 2016 to 2017 was 0.028 W m^{-2} and the total radiative forcing due to all greenhouse gases was 0.034 W m^{-2}.[37] Therefore, the temporary negative radiative forcing due to the increase in stratospheric aerosols after the Nabro and Raikoke volcanic eruptions might have exceeded the annual radiative forcing due to all greenhouse gases.

Stratospheric smoke particles from the 2017 Canadian forest fires were detected by the Saga lidar. The degree of depolarization of smoke particles was about 0.1–0.18, and this value persisted for a long period of time, from 31 August 2017 to 22 February 2018. As shown by the record-breaking wildfires in southeastern Australia in late December 2019 and early January 2020, global warming will increase the influx of smoke particles into the stratosphere due to pyroCb clouds.

Acknowledgements

Lidar operation at Saga is supported in part by the GOSAT series project. We would like to thank S. Takubo, T. Kawasaki, T. Akaho, S. Okano, G. Hamano, and H. Sakaguchi for their lidar observations. The world blank map in Fig. 1 was reproduced from https://happylilac.net/sy-sekaitizu-s3.html.

References

1) M. P. McCormick, L. W. Thomason, and C. R. Trepte, "Atmospheric effects of Mt Pinatubo eruption," Nature, **373**, 399–404 (1995), https://doi.org/10.1038/373399a0.

2) S. Solomon, K. Dube, K. Stone, P. Yu, D. Kinnison, O. B. Toon, S. E. Strahan, K. H. Rosenlof, R. Portmann, S. Davis, W. Randel, P. Bernath, C. Boone, C. G. Bardeen, A. Bourassa, D. Zawada, and D. Degenstein, "On the stratospheric chemistry of midlatitude wildfire smoke," Proc. Natl. Acad. Sci. USA., **119**, e2117325119, (2022), https://doi.org/10.1073/pnas.2117325119.

3) N. Trieu, I. Morino, O. Uchino, Y. Tsutsumi, T. Sakai, T. Nagai, A. Yamazaki, H. Okumura, K. Arai, K. Shiomi, D. F. Pollard, and B. Liley, "Influences of aerosols and thin cirrus clouds on GOSAT XCO_2 and XCH_4 using Total Carbon Column Observing Network, sky radiometer, and lidar data," Int. J. Rem. Sens., **43**, 1770–1799 (2022), https://doi.org/10.1080/01431161.2022.2038395.

4) C. W. O'Dell, A. Eldering, P. O. Wennberg, D. Crisp, M. R. Gunson, B. Fisher, C. Frankenberg, M. Kiel, H. Lindqvist, L. Mandrake, A. Merrelli, V. Natraj, R. R. Nelson, G. B. Osterman, V. H. Payne, T. E. Taylor, D. Wunch, B. J. Drouin, F. Oyafuso, A. Chang, J. McDuffie, M. Smyth, D. F. Baker, S. Basu, F. Chevallier, S. M. R. Crowell, L. Feng, P. I. Palmer, M. Dubey, O. E. García, D. W. T. Griffith, F. Hase, L. T. Iraci, R. Kivi, I. Morino, J. Notholt, H. Ohyama, C. Petri, C. M. Roehl, M. K. Sha, K. Strong, R. Sussmann, Y. Te, O. Uchino, and V. A. Velazco, "Improved retrievals of carbon dioxide from Orbiting Carbon Observatory-2 with the version 8 ACOS algorithm," Atmos. Meas. Tech., **11**, 6539–6576 (2018), https://doi.

org/10.5194/amt-11-6539-2018.

5) O. Uchino, T. Sakai, T. Nagai, K. Nakamae, I. Morino, K. Arai, H. Okumura, S. Takubo, T. Kawasaki, Y. Mano, T. Matsunaga, and T. Yokota, "On recent (2008–2012) stratospheric aerosols observed by lidar over Japan," Atmos. Chem. Phys., **12**, 11975–11984 (2012), https://doi.org/10.5194/acp-12-11975-2012.

6) O. Uchino, T. Sakai, T. Izumi, T. Nagai, I. Morino, A. Yamazaki, M. Deushi, K. Yumimoto, K., T. Maki, T. Y. Tanaka, T. Akaho, H. Okumura, K. Arai, T. Nakatsuru, T. Matsunaga, and T. Yokota, "Lidar detection of high concentrations of ozone and aerosol transported from northeastern Asia over Saga, Japan," Atmos. Chem. Phys., **17**, 1865–1879 (2017),. https://doi.org/10.5194/acp-17-1865-2017.

7) S. Kobayashi, Y. Ota, Y. Harada, A. Ebita, M. Moriya, H. Onoda, K. Onogi, H. Kamahori, C. Kobayashi, H. Endo, K. Miyaoka, and K. Takahashi, "The JRA-55 Reanalysis: General specifications and basic characteristics," J. Meteor. Soc. Japan, **93**, 5–48 (2015), https://doi.org/10.2151/jmsj.2015-001.

8) WOUDC - World Ozone and Ultraviolet Radiation Data Centre, https://woudc.org/home.php(Accessed 2023.10.11)

9) H. Jäger and T. Deshler, "Correction to "Lidar backscatter to extinction, mass and area conversions for stratospheric aerosols based on midlatitude balloonborne size distribution measurements"," Geophys. Res. Lett., **30**(7), 1382 (2003), https://doi.org/10.1029/2003GL017189.

10) J.-P. Vernier, J. P. Pommereau, A. Garnier, J. Pelon, N. Larsen, J. Nielsen, T. Christiansen, F. Cairo, L. W. Thomason, T. Leblanc, and I. S. McDermid, "Tropical stratospheric aerosol layer from CALIPSO lidar observations," J. Geophys. Res., **114**, D00H10 (2009), https://doi.org/10.1029/2009JD011946.

11) J. Kar, M. A. Vaughan, K.-P Lee, J. L. Tackett, M. A. Avery, A. Garnier, B. J. Getzewich, W. H. Hunt, D. Josset, Z. Liu, P. L. Lucker, B. Magill, A. H. Omar, J. Pelon, R. R. Rogers, T. D. Toth, C. R. Trepte, J.-P. Vernier, D. M. Winker, and S. A. Young, "CALIPSO lidar calibration at 532 nm: version 4 nighttime algorithm," Atmos. Meas. Tech., **11**, 1459–1479 (2018), https://doi.org/10.5194/amt-11-1459-2018.

12) J. Kar, K.-P. Lee, M. A. Vaughan, J. L. Tackett, C. R. Trepte, D. M. Winker, P. L. Lucker, and B. J. Getzewich, "CALIPSO level 3 stratospheric aerosol profile product: version 1.00 algorithm description and initial assessment," Atmos. Meas. Tech., **12**, 6173–6191 (2019), https://doi.org/10.5194/amt-12-6173-2019.

13) F. G. Fernald, "Analysis of atmospheric lidar observations: some comments," Appl. Opt., **23**, 652–653 (1984), https://doi.org/10.1364/AO.23.000652.

14) V. Freudenthaler, M. Esselborn, M. Wiegner, B. Heese, M. Tesche, A. Ansmann, D. Müller, D. Althausen, M. Wirth, A. Fix, G. Ehret, P. Knippertz, C. Toledano, J. Gasteiger, M. Garhammer, and M. Seefeldner, "Depolarization ratio profiling at several wavelengths in pure Saharan dust during SAMUM 2006," Tellus B, **61**, 165–179 (2009), https://doi.org/10.1111/j.1600-0889.2008.00396.x.

15) A. Behrendt and T. Nakamura, "Calculation of the calibration constant of polarization lidar and its dependency on atmospheric temperature," Opt. Express, **10**, 805–817 (2002).

16) L. Clarisse, D. Hurtmans, C. Clerbaux, J. Hadji-Lazaro, Y. Ngadi, and P.-F. Coheur, "Retrieval of sulphur dioxide from the infrared atmospheric sounding interferometer(IASI)," Atmos. Meas. Tech., **5**, 581–594 (2012), https://doi.org/10.5194/amt-5-581-2012.

17) T. Sakai, O. Uchino, T. Nagai, B. Liley, I. Morino, and T. Fujimoto, "Long-term variation of stratospheric aerosols observed with lidars over Tsukuba, Japan, from 1982 and Lauder, New Zealand, from 1992 to 2015," J. Geophys. Res.-Atmos., **121**, 10283–10293 (2016), https://doi.org/10.1002/2016JD025132.

18) L. O. Muser, G. A. Hoshyaripour, J. Bruckert, Á. Horváth, E. Malinina, S. Wallis, F. J. Prata, A. Rozanov, C. von Savigny, H. Vogel, and B. Vogel, "Particle aging and aerosol-radiation interaction affect volcanic plume dispersion: evidence from the Raikoke 2019 eruption," Atmos. Chem. Phys., **20**, 15015–15036 (2020), https://doi.org/10.5194/acp-20-15015-2020.

19) J. de Leeuw, A. Schmidt, C. S. Witham, N. Theys, I. A. Taylor, R. G. Grainger, R. J. Pope, J. Haywood, M. Osborne, and N. I. Kristiansen, "The 2019 Raikoke volcanic eruption-Part 1: Dispersion model simulations and satellite retrievals of volcanic sulfur dioxide," Atmos. Chem. Phys., **21**, 10851–10879 (2021), https://doi.org/10.5194/acp-21-10851-2021.

20) Z. Cai, S. Griessbach, and L. Hoffmann, "Improved estimation of volcanic SO_2 injections from satellite retrievals and Lagrangian transport simulations: the 2019 Raikoke eruption," Atmos. Chem. Phys., **22**, 6787–6809 (2022), https://doi.org/10.5194/acp-22-6787-2022.

21) C. Kloss, G. Berthet, P. Sellitto, F. Ploeger, G. Taha, M. Tidiga, M. Eremenko, A. Bossolasco, F. Jégou, J.-B. Renard, and B. Legras, "Stratospheric aerosol layer perturbation caused by the 2019 Raikoke and Ulawun eruptions and their radiative forcing," Atmos. Chem. Phys., **21**, 535–560 (2021), https://doi.org/10.5194/acp-21-535-2021.

22) G. Vaughan, D. Wareing, and H. Ricketts, "Measurement Report: Lidar measurements of stratospheric aerosol following the 2019 Raikoke and Ulawun volcanic eruptions," Atmos. Chem. Phys., **21**, 5597–5604(2021), https://doi.org/10.5194/acp-21-5597-2021.

23) F. Chouza, T. Leblanc, J. Barnes, M. Brewer, P. Wang, and D. Koon, "Long-term (1999–2019) variability of stratospheric

aerosol over Mauna Loa, Hawaii, as seen by two co-located lidars and satellite measurements," Atmos. Chem. Phys., **20**, 6821–6839 (2020), https://doi.org/10.5194/acp-20-6821-2020.

24) M. Fromm, R. Bevilacqua, R. Servranckx, J. Rosen, J. P. Thayer, J. Herman, and D. Larko, "Pyro-cumulonimbus injection of smoke to the stratosphere: Observations and impact of a super blowup in northwestern Canada on 3–4 August 1998," J. Geophys. Res.-Atmos., **110**, D08205 (2005), https://doi.org/10.1029/2004JD005350.

25) D. A. Peterson, J. R. Campbell, E. J. Hyer, M. D. Fromm, G. P. Kablick, J. H. Cossuth, and M. T. DeLand, "Wildfire-driven thunderstorms cause a volcano-like stratospheric injection of smoke," npj Clim. Atmos. Sci., **1**, 30 (2018), https://doi.org/10.1038/s41612-018-0039-3.

26) A. Ansmann, H. Baars, A. Chudnovsky, I. Mattis, I. Veselovskii, M. Haarig, P. Seifert, R. Engelmann, and U. Wandinger, "Extreme levels of Canadian wildfire smoke in the stratosphere over central Europe on 21–22 August 2017," Atmos. Chem. Phys., **18**, 11831–11845 (2018), https://doi.org/10.5194/acp-18-11831-2018.

27) S. M. Khaykin, S. Godin-Beekmann, A. Hauchecorne, J. Pelon, F. Ravetta, and P. Keckut, "Stratospheric smoke with unprecedentedly high backscatter observed by lidars above southern France," Geophys. Res. Lett., **45**, 1639–1646 (2018), https://doi.org/10.1002/2017GL076763.

28) V. V. Zuev, V. V. Gerasimov, A. V. Nevzorov, and E. S. Savelieva, "Lidar observations of pyrocumulonimbus smoke plumes in the UTLS over Tomsk (Western Siberia, Russia) from 2000 to 2017," Atmos. Chem. Phys., **19**, 3341–3356 (2019), https://doi.org/10.5194/acp-19-3341-2019.

29) P. Yu, O. B. Toon, C. G. Bardeen, Y. Zhu, K. H. Rosenlof, R. W. Portmann, T. D. Thornberry, R. S. Gao, S. M. Davis, E. T. Wolf, J. de Gouw, D. A. Peterson, M. D. Fromm, and A, Robock, "Black carbon lofts wildfire smoke high into the stratosphere to form a persistent plume," Science, **365**, 587–590 (2019), https://doi.org/10.1126/science.aax1748.

30) M. Haarig, A. Ansmann, H. Baars, C. Jimenez, I. Veselovskii, R. Ronny Engelmann, and D. Althausen, "Depolarization and lidar ratios at 355, 532, and 1064 nm and microphysical properties of aged tropospheric and stratospheric Canadian wildfire smoke," Atmos. Chem. Phys., **18**, 11847–11861 (2018), https://doi.org/10.5194/acp-18-11847-2018.

31) Q. Hu, P. Goloub, I. Veselovskii, J.-A. Bravo-Aranda, I. E. Popovici, T. Podvin, M. Haeffelin, A. Lopatin, O. Dubovik, C. Pietras, X. Huang, B. Torres, and C. Chen, "Long-range transported Canadian smoke plumes in the lower stratosphere over northern France," Atmos. Chem. Phys., **19**, 1173–1193 (2019), https://doi.org/10.5194/acp-19-1173-2019.

32) O. Uchino, "Scientific results of the EPIC projects," NATO ASI Ser., **142**, 127–139 (1996),

33) L. L. Stowe, L. L. Carey, and P. P. Pellegrino, "Monitoring the Mt. Pinatubo aerosol layer with NOAA/11 AVHRR data," Geophys. Res. Lett., **19**, 159–162 (1992), https://doi.org/10.1029/91GL02958.

34) H. Jäger, O. Uchino, T. Nagai, T. Fujimoto, V. Freudenthaler, and F. Homburg, "Ground-based remote sensing of the decay of the Pinatubo eruption cloud at three Northern Hemisphere sites," Geophys. Res. Lett., **22**, 607–610 (1995), https://doi.org/10.1029/95GL00054.

35) J. Hansen, M. Sato, R. Ruedy, L. Nazarenko, A. Lacis, G. A. Schmidt, G. Russell, I. Aleinov, M. Bauer, S. Bauer, N. Bell, B. Cairns, V. Canuto, M. Chandler, Y. Cheng, A. Del Genio, G. Faluvegi, E. Fleming, A. Friend, T. Hall, C. Jackman, M. Kelley, N. Kiang, D. Koch, J. Lean, J. Lerner, K. Lo, S. Menon, R. Miller, P. Minnis, T. Novakov, V. Oinas, J. Perlwitz, J. Perlwitz, D. Rind, A. Romanou, D. Shindell, P. Stone, S. Sun, N. Tausnev, D. Thresher, B. Wielicki, T. Wong, M. Yao, and S. Zhang, "Efficacy of climate forcings," J. Geophys. Res., **110**, D18104 (2005), https://doi.org/10.1029/2005JD005776.

36) S. Solomon, J. S. Daniel, R. R. Neely III, J.-P. Vernier, E. G. Dutton, and L. W. Thomason, "The persistently variable "background" stratospheric aerosol layer and global climate change," Science, **333**, 866–870 (2011), https://doi.org/10.1126/science.1206027.

37) NOAA, "The NOAA Annual Greenhouse Gas Index(AGGI)," https://gml.noaa.gov/aggi/aggi.html (Accessed 2023.10.11).

Author Introduction

Corresponding author: Osamu Uchino
Doctor of Science, Kyushu University, Fukuoka, Japan. Visiting researcher at the Meteorological Research Institute.

Paper

Journal of Laser Radar Society of Japan, Vol. 5, No. 1 (2024)

Full-parameter performance simulation theory for velocity azimuth display pulsed coherent Doppler lidar, and error analysis on wind speed measurement in shear flow

Shumpei Kameyama*[1]

[1]*Mitsubishi Electric Corporation, Information Technology R&D Center, 5-1-1 Ofuna,*
Kamakura, Kanagawa, Japan 247-8501

(Received December 05, 2023; revised February 3, 2024; accepted February 19, 2024)

Full-parameter performance simulation theory is shown for velocity azimuth display pulsed coherent Doppler lidar (VAD-PCDL). The parameters include not only VAD-PCDL parameters but also atmospheric ones. Influences of these parameters regarding range-dependent intensity of heterodyne-detected signal and digital signal processing are considered. The simulation theory can be applied for general wind field cases. Example analysis of wind speed measurement error is shown for the case of sheared wind flow. Some cases of the vertical wind profiles with shear are set for the input, and wind speed measurement using VAD scan is performed using the fast Fourier transform (FFT) based signal processing. Approach of Monte-Carlo computer simulation is applied. With this method, we analyze the wind speed measurement error caused by factors of (i) shear curvature, (ii) signal-to-noise (SNR) weighting, and (iii) height sensing error.

Key Words: Coherent Doppler lidar, Wind speed measurement, Shear flow

1. Introduction

Recent growing of wind energy industry needs larger wind turbines with higher hub heights. Under this background, wind resource assessments at higher heights become more important in advance of wind farm constructions with large wind turbines. This causes the necessity of extremely tall meteorological masts for traditional wind resource assessments using cup anemometers. To prevent the above-mentioned necessity, a coherent Doppler lidar (CDL)[1–7] has been attractive since this device realizes remote wind sensing from the ground. Especially, the velocity azimuth display pulsed CDL (VAD-PCDL)[8, 9] provides vertical profiling of horizontal wind speed. A VAD-PCDL can be an alternative to a meteorological mast, even though it is still under discussed by the wind energy community if it can be a full replacement. The performances of VAD-PCDLs have been evaluated for the wind resource assessments in several measurement campaigns[8–15]. Further, activities on this application toward international standardization have been carried on, and some recommended practices have been published by the international energy agency (IEA) task[16, 17]. A VAD-PCDL is now a recognized device for wind resource assessments. However, there are some remaining issues toward wider application of wind resource assessments using VAD-PCDLs. One of the issues is understanding the influence of probe volume on wind measurement in inhomogeneous flow. A VAD-PCDL measures a weighted averaged wind speed within a probe volume even though a cup anemometer measures a wind speed at a certain point. This difference potentially causes measurement error for a VAD-PCDL if a wind speed at a certain point is defined as a true value. There are several kinds of inhomogeneous flow, for example, horizontal shear, wakes, and so on. Wind speed measurement errors of VAD-PCDLs with a set of fixed CDL parameters have been evaluated in several measurement campaigns under several wind flow conditions[8–15]. However, only few works have been performed for the influences of CDL parameters in these flows.

The influences of pulse shape (i.e., time profile of transmitting pulse energy of CDL) in wakes and horizontal shear have been studied[18, 19], but parameters which determine the range-dependent intensity of heterodyne-detected signal have not been considered. In addition, the influence of digital signal processing has not included in these works. For VAD-PCDLs, several parameters (for example, beam focusing distance, atmospheric transmittance, etc.) impact the range-dependent intensity of heterodyne-detected signal. Further, parameters for digital signal processing (time gate width, line-of-sight (LOS) wind velocity estimation algorithm, etc.) impact wind speed measurement accuracy. Therefore, simulation method for error analysis using more detailed model has been necessary for the understanding of VAD-PCDL measurement.

In this paper, the performance simulation theory with full VAD-PCDL parameters is shown. Example analysis of wind speed measurement error is shown for the case of sheared wind flow. Although the influence of pulse shape has been considered in complex flow (i.e., wakes)[19], simpler wind flow of horizontal shear is assumed here. The understanding of measurement error in shear flow is very important, since it is one of representative and the most basic wind field in wind resource assessments.

In the simulation of this paper, the model of the received signal (heterodyne-detected signal of a PCDL) is expressed as the summation of incoherent backscattered signals from the thin sliced atmospheric ranges and detector noise. The speckle effect, which is a feature of a PCDL signal, can be modelled by the above-mentioned summation. The intensity of the received signal from each sliced range is weighted using the signal to noise ratio (SNR) equation. Full PCDL parameters, including the pulse shape, range resolution, and focal range of laser beam, are considered in the simulation. The atmospheric conditions, including the atmospheric transmission, backscatter coefficient, and wind profile, are also considered. Some cases of the vertical wind profiles with shear are set for the input. Ideal horizontal wind profiles with vertical shear are assumed. Wind speed measurement using VAD scan is simulated using the fast Fourier transform (FFT) based signal processing in the Monte-Carlo method. Using this simulation, we analyze the wind speed measurement error caused by factors of (i) shear curvature, (ii) SNR weighting, and (iii) height sensing error.

The rest of this paper is organized as follows. Basic configuration and operation of a VAD-PCDL are shown in section 2. Model of heterodyne-detected signal is described in section 3. Simulation procedure for error analysis is explained in section 4. Error sources are shown in section 5. Simulation parameters and results with some investigations are introduced in section 6 and 7. Comparison with past work is shortly investigated in section 8. Some parts of this paper have been presented in the 18th international symposium for advancement of boundary-layer remote sensing (ISARS) in 2016, but the proceedings had not been published because of unknown reasons. Minor differences exist regarding the simulation results between the previous presentation and this paper because of some correction on the detailed simulation. Further, detail explanations and new simulation results are newly shown in this paper.

2. VAD-PCDL

The configuration of a VAD-PCDL is schematically shown in Fig. 1. The detail of each component is not explained here since this is outside the scope of this paper (for more detail, see an example[7]). A continuous wave laser light is transmitted and divided. A part of the divided light is sent to a balanced receiver as a local light. The other part is pulse modulated, amplified, and transmitted to the atmosphere through an optics. The backscattered light from aerosols in the atmosphere is received through the same optics and a circulator. The received light is heterodyne-detected with the local light by the balanced receiver. The heterodyne-detected signal is analogue-to-digital (A/D) converted and is processed by a signal processor, and a range dependence of line-of-sight wind velocity is estimated using range gating and spectral analysis using FFT and incoherent spectrum accumulation. The LOS wind velocity is estimated as the first moment of the spectrum, which is given by

$$V_{LOS} = \frac{\lambda}{2MT_S}\left(\frac{\sum_{i=p-w}^{p+w}\left[(i-p)\cdot S(i)\right]}{\sum_{i=p-w}^{p+w} S(i)}\right), \qquad (1)$$

where λ is the laser wavelength (m), M is the sample number in a range gate, T_S is the sampling interval, $S(i)$ is the spectrum obtained by FFT (a.u.), i is the frequency bin number, p is the peak frequency bin, and w is the width used for the first-moment operation. The FFT-based LOS wind velocity estimation with the above-mentioned moment operation

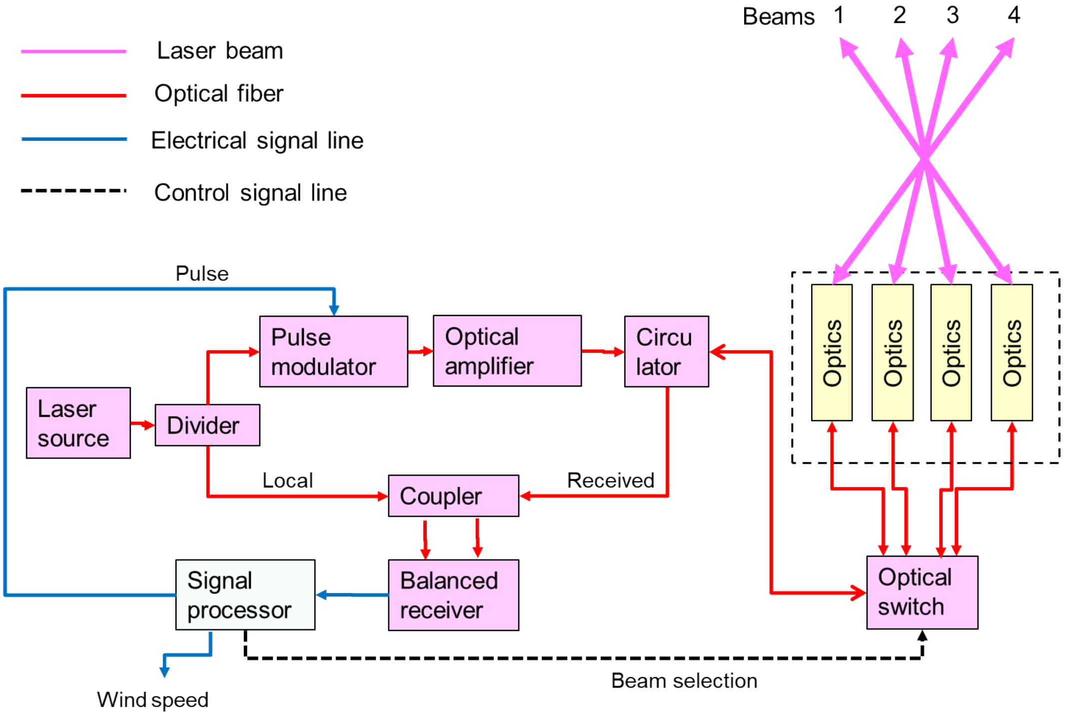

Fig. 1 Schematic of VAD-PCDL configuration.

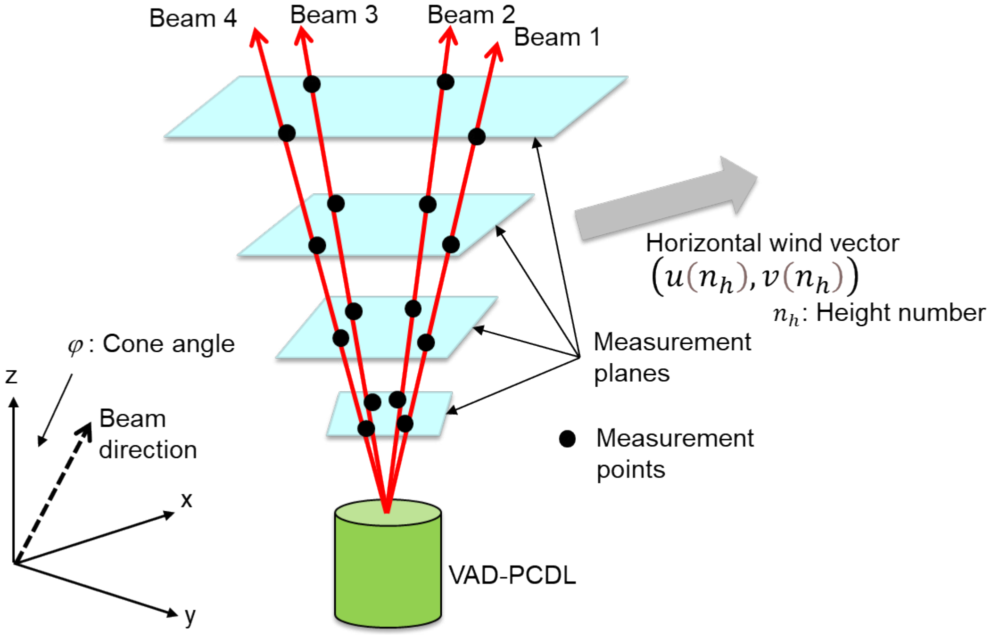

Fig. 2 Schematic of VAD measurement.

is influenced by shear flow or turbulence within a probe volume. However, this estimation method is an authentic one for processing of weather echoes[20)], and it is widely used for the existing CDLs[9, 10)] because of the merit of real-time processing and the high signal detection ability.

The VAD-PCDL in the figure has four beams with 90 degrees interval for circumferential direction. The above-mentioned configuration with fiber-based circuit is basically same as the ones in[6, 7, 9)]. The line-of-sight (LOS) wind velocity is obtained for each beam with changing selected beam (from 1 to 4).

The schematic of wind speed measurement for a VAD-PCDL is shown in Fig. 2. Wind speed vector at a certain height (($u(n_h)$, $v(n_h)$), n_h: height number of range gates) are obtained by assuming homogeneous wind field as[9, 15]

$$u\,(n_h) = \frac{V_{L2}\,(n_h) - V_{L4}\,(n_h)}{2\sin\varphi}, \qquad (2)$$

$$v\,(n_h) = \frac{V_{L1}\,(n_h) - V_{L3}\,(n_h)}{2\sin\varphi}, \qquad (3)$$

where $V_{Lb}(n_h)$ is the LOS velocity (m/s) of the beam number b (= 1, 2, 3, 4), and φ is the cone angle (rad). The vertical wind component can be obtained using velocities of the beam 1,3 or 2,4 but is not considered here.

The horizontal wind speed and direction are calculated by[9, 15]

$$V_h\,(n_h) = \sqrt{u\,(n_h)^2 + v\,(n_h)^2}\,, \qquad (4)$$

$$\theta_h\,(n_h) = tan^{-1}\frac{v\,(n_h)}{u\,(n_h)}. \qquad (5)$$

3. Model of heterodyne-detected signal

Here, a heterodyne-detected signal is expressed as the summation of incoherent backscattered signals from sliced atmospheric ranges and detector noise. This model is denoted in Fig. 3. The model of a heterodyne-detected signal is the one which has been denoted in past literatures[21, 22], and it is combined with the SNR equation[23, 24]. The validity of the signal model has been confirmed in comparison with actual CDL data[21]. The SNR equation has been evaluated experimentally in the past[6, 22]. In general, a heterodyne-detected signal with an intermediate frequency and complex time samples are generated using an in-phase quadrature (IQ) detector and two channel A/D converters. Consequently, the signal in the digital domain is expressed as[22]

$$\begin{aligned} S\,(m, i_{IT}) = &\sqrt{\frac{2\sqrt{ln\,2}\,T_S}{\sqrt{\pi}\Delta t}} \\ &\cdot \sum_{\tau=0}^{P}\left\{x\,(\tau, i_{IT})\exp\left\{j\left[\frac{4\pi V_L\,(\tau)}{\lambda}\,(m-1)\,T_S\right]\right\}\ \times\exp\left(-2\,ln\,2\cdot\frac{(m\cdot T_S\ - 2\tau\Delta L/c)^2}{\Delta t^2}\right)\cdot\sqrt{SNR\,(\tau)}\right\} \\ &+ N_{oise}\,(m, i_{IT})\,, \qquad (6) \end{aligned}$$

where m denotes the sample number corresponding to the time; i_{IT}, the iteration number in the Monte-Carlo simulations; τ, the sliced atmospheric range number; Δt, the Full Width Half Maximum (FWHM) of the transmitting pulse (s) ; ΔL, the length of the sliced atmospheric range; and c, the speed of light (m/s). SNR (τ) denotes the SNR at range number τ, which is the signal-to-noise ratio of the average signal power to the average noise power. $\mathrm{N}_{\mathrm{oise}}\,(m, i)$ denotes the complex amplitude of the white Gaussian detector noise having normalized average power of 1, and x (τ, i) denotes the complex amplitude of the signal from each atmospheric range and the complex statistically independent zero mean Gaussian variable with normalized average power of 1. This statistical property expresses the speckle effect of the signals. $V_L(\tau)$ denotes the line-of-sight (LOS) wind velocity of each sliced range (m/s) which corresponds to the assumed wind field. In the cases of a VAD-PCDL and ideal horizontal wind field (zero vertical wind), the LOS velocity is obtained by the projection of the horizontal wind speed to the LOS direction. P is the number of the sliced atmospheric ranges considered in the simulation should be considerably larger than the simulated range region. It is assumed that the SNR is constant in the above-mentioned atmospheric slices ranges and the spectrum of the transmitting pulse is the Fourier transform limit. It should be noted that only envelopes (i.e., intensity profiles) of signals from the sliced atmospheric ranges are shown in Fig. 3, but the summation of these signals is performed in complex (i.e., electrical field) domain. This point is expressed in eq. (6).

The SNR, which is proportional to the range-dependent intensity of heterodyne-detected signal, determines the range-dependent weighting of the signal in eq. (6), and is expressed as[24]

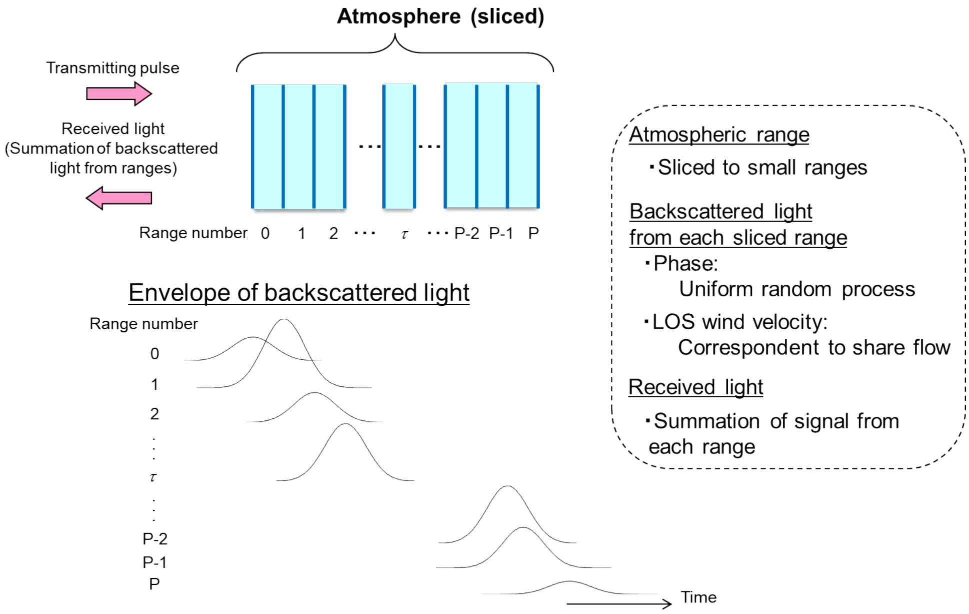

Fig. 3 Schematic of signal from sliced atmospheric ranges. Each sliced range has a wind speed corresponding to a wind field.

$$SNR(\tau) = \frac{\eta_D(L)\,\lambda E \beta K^{2L/1000} \pi D^2}{8hBL^2}, \qquad (7)$$

where h is Planck's constant (Js), E is the transmitting pulse energy (J), D is the receiving aperture diameter (m), L is the range (m) ($=\tau\Delta L$), which is given by $L = z/\cos\varphi$, where z is the height (m). B is the receiver bandwidth (Hz), β is the atmospheric backscatter coefficient (m^{-1} sr^{-1}), and K is the atmospheric transmittance (km^{-1}). η_D is the system efficiency given by[24)]

$$\eta_D(L) = \frac{\eta_F}{\left\{1 + \left(1 - \frac{L}{L_F}\right)^2 \left[\frac{\pi (A_C D)^2}{4\lambda L}\right]^2 + \left(\frac{A_C D}{2S_0(L)}\right)^2\right\}}, \qquad (8)$$

where A_C is the correction factor, and the approximated diameter of the transmitting beam is $A_c D$[24)]. η_F is the far-field system efficiency. $S_0(L)$ is the transverse coherent length (m), and if the refractive index structure constant ($C_n{}^2$(m$^{-2/3}$)) is constant along the beam path, $S_0(L)$ is approximated by $(1.1k^2 L C_n{}^2)^{-3/5}$ where k is the wave number ($=2\pi/\lambda$). L_F is the focal range of the transmitting beam (m). In cases of VAD-PCDL, this parameter is given by $L_F = L_h/cos\varphi$, where L_h is the beam focusing height (m). The equations (7) and (8) show that the range dependence of SNR weighting is expressed by complex combination of several terms. These are (i) optical attenuation in the atmosphere (in numerator of eq. (7), which is caused by optical extinction and absorption), (ii) diffuse attenuation regarding aerosol scattering (L^2 in denominator of eq. (7)), (iii) beam focusing effect (in second term of denominator of eq. (8)), (iv) aberration caused by refractive turbulence (in third term of denominator of eq. (8)), and (v) receiving aperture diameter (in second and third term of denominator in eq. (8)).

The wind field is assumed to be ideal horizontal wind and has the simple power low formulation as[18)]

$$U(z) = U_0 \left(\frac{z}{z_0}\right)^{\alpha}, \qquad (9)$$

where z_0 is the reference height (m), U_0 is the reference speed (m/s)which is set as a deterministic value, and α is the shear exponent of the horizontal wind speed. The LOS velocity in eq. (6) can be obtained using this equation and the cone angle in the VAD measurement. Several shear behaviors can appear under different atmospheric stability conditions. However, the assumption of eq. (9) is suitable for the basis of understanding and this expression has been used in several wind field analysis[25, 26)]. The simulation for other shear models can be possible by simply substituting the wind field instead of eq. (9).

4. Simulation procedure

Schematic of simulation procedure is shown in Fig. 4. Since the signal model of eq. (6) includes the random process, the Monte-Carlo simulation is used. The parameters which has the random process in eq. (6) are $x(\tau, i)$, SNR(τ), and N_{oise} (m, i). A heterodyne-detected signal is generated by a computer, according to (6) and the random process described in section 3. Then, the signal is range-gated, and signal processing and velocity estimation are performed according to the algorithm corresponding to the selected velocity estimator. The schematic of the simulated heterodyne-detected signal and signal processing is denoted in Fig. 5. In the figure, N is the range gate number for the signal processing corresponding to the wind sensing ranges (which is different from the sliced atmospheric range number: τ). Following the

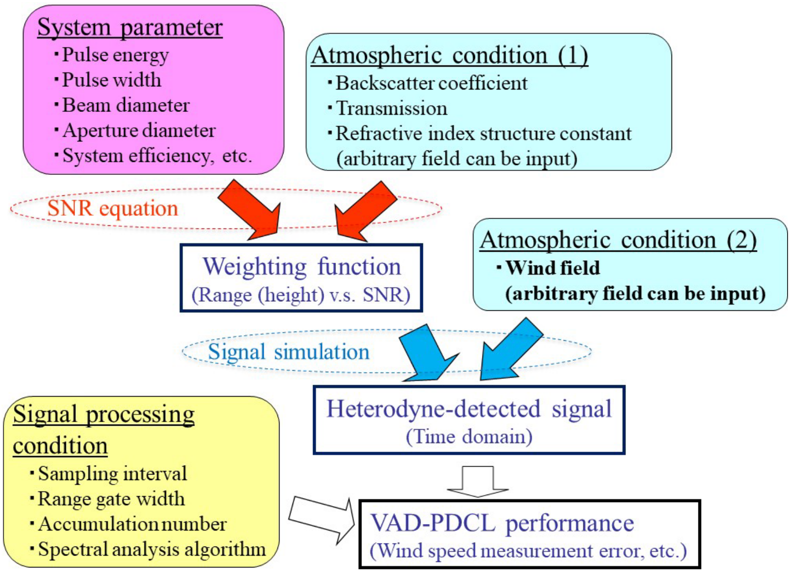

Fig. 4 Schematic of simulation procedure.

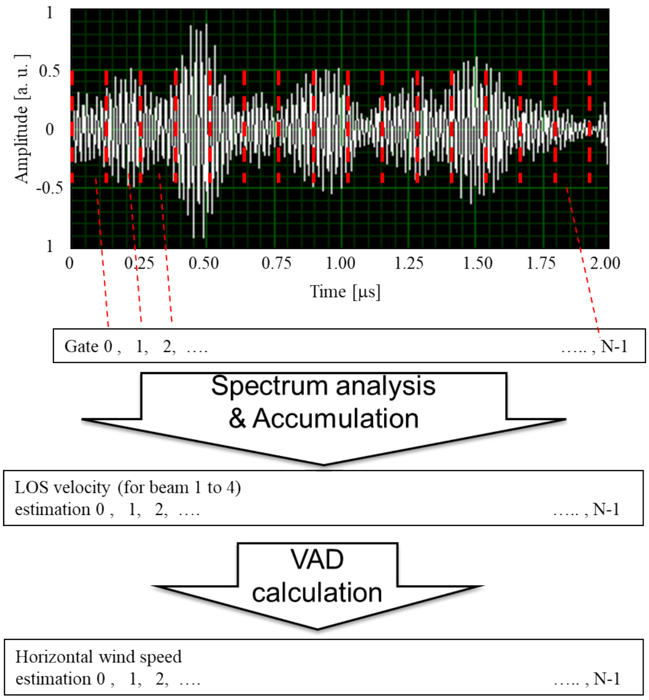

Fig. 5 Schematic of the simulated heterodyne-detected signal and signal processing.

iterations of this simulation procedure, the periodogram (i.e. spectrum) is accumulated and the LOS velocity is obtained using the pre-determined method. The four direction (90 degrees interval) VAD is considered. The wind direction is assumed to be constant regarding its height profile and also to be the same as the horizontally projected vector of the two of the beams.

5. Error sources

Basically, wind speed measurement error for VAD-PCDL is caused by asymmetry regarding wind profile and/or SNR weighting within a probe volume. The following three factors are considered. These are schematically shown in Fig. 6.

- Shear curvature (Fig. 6(a)) : The error caused by this factor is expressed as ‘Δ_C’ and given in per cent $(=(U_l - U_t)/U_t \cdot 100)$ where U_l is the horizontal wind speed measured by a VAD-PCDL and U_t is the true horizontal wind speed at the nominal height which is given by eq. (6).
- SNR weighting (Fig. 6(b)) : This error is caused by the combined effect of the shear curvature and the SNR weighting. This is expressed as ‘Δ_S’ and also given in percent. In general, the weighting has a peak value around the beam focusing height and decreases for other height region owing to the defocusing characteristic of eq. (7) and (8). For larger heights, the decreasing is more distinct owing to many sources (optical attenuation in the atmosphere, etc.).
- Height sensing error (Fig. 6(c)) : This error is caused by the combined effect of the shear curvature, the SNR weighting, and +0.65 m of sensing height error (i.e., sensing at 80.65 m instead of 80 m). The value of 0.65 m corresponds to one sampling interval in Table 2 which is projected from LOS to height direction. This is expressed

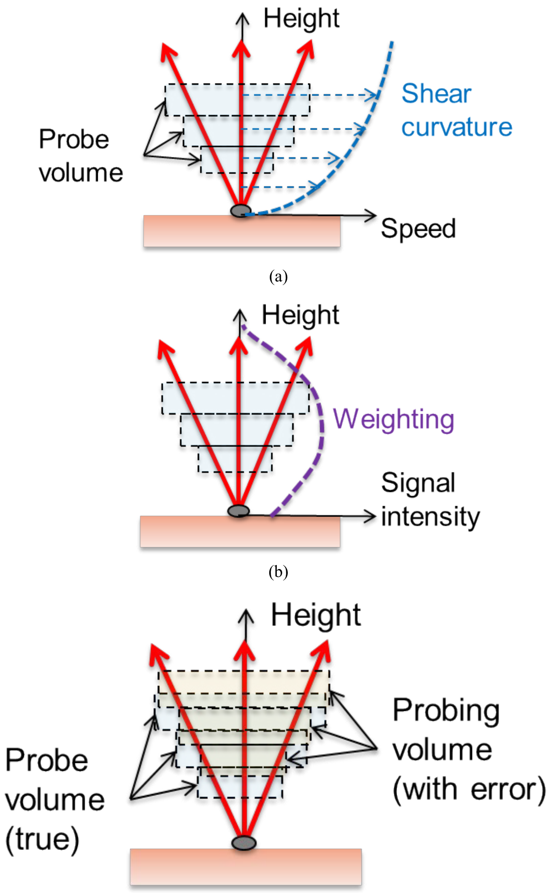

(a)

(b)

(c)

Fig. 6 Schematic of (a) : shear curvature, (b) SNR weighting, and (c) : height sensing error.

Table 1 Factors which are considered in three kinds of errors.

Symbol Factor	Δ_C	Δ_S	Δ_H
Shear curvature	○	○	○
SNR weighting	×	○	○
Height sensing error	×	×	○

as 'Δ_H' and also given in percent.

Factors which are considered in the above-mentioned three errors (Δ_C, Δ_S, and Δ_H) are shown in Table 1.

6. Simulation condition

Simulation parameters are shown in Table 2. Simulations are performed for five shear exponent cases. The range of shear exponent has been set by referencing a past literature[18]. The value of FWHM of the transmitting pulse corresponds to probe length of 20 m. The beam focusing heights of 100 m and 200 m correspond to the focal ranges of transmitting beam of 230.94 m and 115.47 m by considering the beam cone angle. Two receiving aperture diameters of 0.04 m and 0.07 m are considered. The cone angle of $\pi/6$ rad ($=30$ degrees) is assumed. The above-mentioned instrumental parameters are set by referencing existing PCDLs[6, 7, 9]. The above-mentioned variety of parameters causes changes of weighting function (i.e., height dependence of SNR). The height profiles of horizontal wind speed, pulse weighting, and SNR weighting are shown in Fig. 7. The pulse weighting is the same as the pulse shape, and it is projected to the height direction in the figure. This weighting corresponds to volume averaging effect for LOS (or height) direction and

Table 2 Simulation parameters.

Parameter		Value	Unit	Symbol
Physical parameters	Planck's constant	-	Js	h
	Speed of light	-	m/s	c
Atmospheric parameters	Atmospheric backscatter coefficient	-	/m/sr	β
	Atmospheric transmittance	0.90	/km	K
	Atmospheric refractive index structure constant	0	$m^{-2/3}$	C_n^2
Wind condition	Reference height	80.00	m	z_0
	Reference speed	10.00	m/s	U_0
	Shear exponent	0.0, 0.1, 0.2, 0.3		α
Instrumental parameters	Laser wavelength	1.55×10^{-6}	m	λ
	Transmitting pulse energy	-	J	E
	FWHM of the transmitting pulse	1.56×10^{-7}	s	Δt
	Receiving aperture diameter	0.04, 0.07	m	D
	Correction factor	0.71	-	A_C
	Beam focusing height	100, 200	m	L_h
	Receiver bandwidth	-	Hz	B
	Beam cone angle	$\pi/6$	rad	φ
Signal processing parameters	Sampling interval	5×10^{-9}	s	T_S
	Frequency bin width for moment operation	5	-	w
	Sample number in a range gate	32	-	M
Simulation parameters	Spectral accumulation number	50,000	-	-
	Length of the sliced atmospheric range	0.025	m	ΔL
	Number of the sliced atmospheric ranges	16,000	-	P

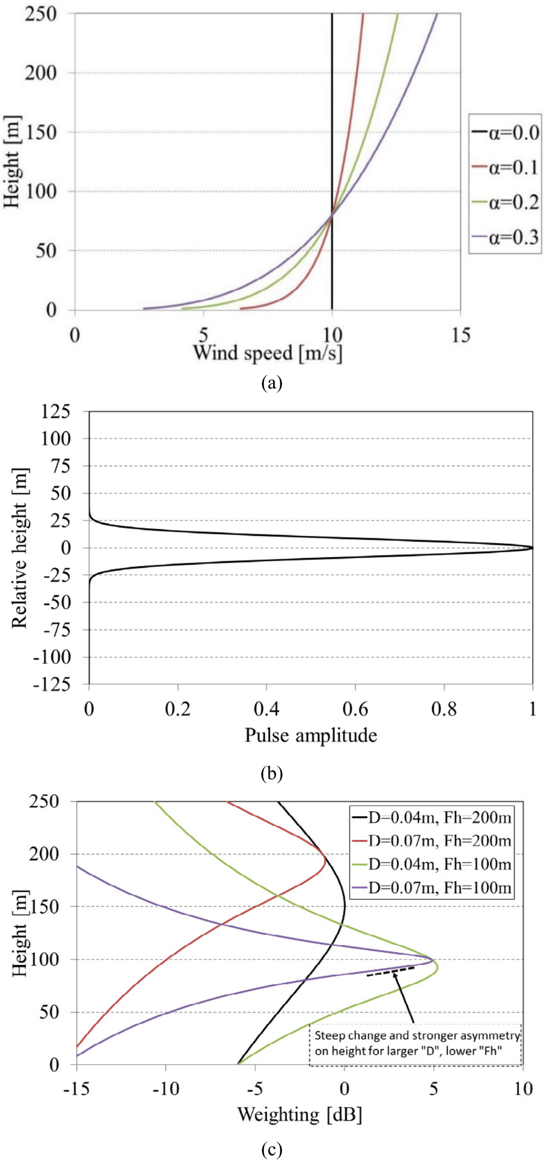

(a)

(b)

(c)

Fig. 7 Height profiles of (a) : Horizontal wind speed, (b) : Pulse weighting, and (c) : SNR weighting. The weighting in (c) is normalized by the maximum value for the case of D = 0.04 m and Fh = 200 m. Tendency on SNR weighting on height is schematically explained in (c).

becomes an error source in wind speed measurement. In some cases (for example, in the case of $D = 0.04$ m and $F_h = 200$ m), SNR weighting does not become maximum at a beam focusing height. This situation tends to appear when the approximated diameter of the transmitting beam (i.e., $A_c D$ in eq. (8), which is proportional to D), is small. In such a case, the beam focusing effect is weak and the range-dependent SNR attenuation in eq. (7) overcomes the beam focusing effect in eq. (8). In general, steep change and stronger asymmetry of SNR weighting appears on height profile for larger D and lower F_h. This is known from eq. (8), and can be seen in Fig. 7(c).

The sampling interval of 5 ns corresponds to the LOS length of 0.75 m. The length of sliced atmospheric range of 0.025 m is set smaller than the sampling interval. The set of sampling interval and sampling number in a range gate determines a range gate width, and it corresponds to the width of 21 m by projection to height direction. FFT is chosen as a velocity estimator. The LOS velocity is obtained from the first moment of the peak in the spectrum which is calculated using FFT. The spectral accumulation number of 50,000 is performed to reduce speckle noise.

The instrumental parameters in Table 2 are just examples. Further discussion is needed for the general case. Further, the detector noise is neglected in the simulation of this paper to reduce the influence of random noise. Therefore, some of the parameters, of which the contribution to SNR is simply proportional (for example, atmospheric backscatter coefficient, transmitting pulse energy, etc.), do not impact the simulation results. The values of these parameters are not denoted in the table. The value of the correction factor is the optimum one for the given diameter of the circular receiving aperture. This corresponds to the case that the $1/e^2$ intensity beam diameter is 80% of the diameter of the aperture.

7. Simulation results

The simulation results regarding the cases in Table 2 and Fig. 7 are shown in tables 3 to 6. True wind speed for each height and each case of shear exponent is additionally shown in the tables. It should be noted that the errors in the tables are relative values in unit of "%" (not "m/s"). If the error values in unit of "m/s" are same for multiple heights, the

Table 3　Results of error analysis ($D = 40$ mm, $F_h = 200$ m).

Shear exponent: α	Height (m)	Δ_C (%)	Δ_S (%)	Δ_H (%)	U_t (m/s)
0.0	40	-0.1	-0.1	0.1	10.000
	80	0.1	0.0	0.0	10.000
	120	0.0	0.1	-0.1	10.000
	150	0.2	0.1	0.1	10.000
	200	0.0	0.0	0.0	10.000
0.1	40	0.0	0.2	0.3	9.330
	80	-0.1	-0.1	0.1	10.000
	120	0.1	0.1	0.1	10.414
	150	-0.1	0.0	0.1	10.649
	200	-0.1	-0.2	0.0	10.960
0.2	40	-0.1	0.3	0.5	8.706
	80	0.0	0.2	0.6	10.000
	120	0.0	0.3	0.3	10.844
	150	-0.1	0.1	0.3	11.340
	200	-0.1	0.0	0.0	12.011
0.3	40	0.2	0.4	0.5	8.122
	80	0.0	0.2	0.5	10.000
	120	0.1	0.3	0.3	11.293
	150	-0.1	0.2	0.3	12.075
	200	0.0	-0.1	0.0	13.163

Table 4　Results of error analysis ($D = 40$ mm, $F_h = 100$ m).

Shear exponent: α	Height (m)	Δ_C (%)	Δ_S (%)	Δ_H (%)	U_t (m/s)
0.0	40	-0.1	0.2	-0.1	10.000
	80	0.1	-0.1	-0.1	10.000
	120	-0.2	0.2	0.1	10.000
	150	0.1	-0.1	-0.1	10.000
	200	-0.2	-0.1	-0.1	10.000
0.1	40	-0.2	0.3	0.3	9.330
	80	0.0	0.4	0.6	10.000
	120	-0.2	-0.2	-0.4	10.414
	150	0.0	-0.2	0.0	10.649
	200	-0.1	0.0	0.1	10.960
0.2	40	-0.2	0.6	1.0	8.706
	80	0.1	0.8	1.0	10.000
	120	0.1	-0.6	-0.7	10.844
	150	-0.1	-0.2	-0.2	11.340
	200	-0.1	0.0	-0.1	12.011
0.3	40	-0.1	0.7	1.6	8.122
	80	0.0	1.4	1.6	10.000
	120	0.1	-1.0	-0.6	11.293
	150	0.1	-0.4	-0.1	12.075
	200	-0.1	-0.1	-0.1	13.163

Table 5 Results of error analysis ($D = 70$ mm, $F_h = 200$ m).

Shear exponent: α	Height (m)	Δ_C (%)	Δ_S (%)	Δ_H (%)	U_t (m/s)
0.0	40	0.0	-0.1	0.0	10.000
	80	-0.1	-0.1	-0.1	10.000
	120	0.1	0.2	0.1	10.000
	150	-0.1	-0.2	-0.1	10.000
	200	-0.1	0.0	0.0	10.000
0.1	40	0.0	0.0	0.2	9.330
	80	0.2	0.2	0.2	10.000
	120	0.0	0.2	0.3	10.414
	150	0.2	-0.1	0.0	10.649
	200	0.0	-0.1	0.0	10.960
0.2	40	0.0	0.2	0.5	8.706
	80	0.0	-0.1	0.3	10.000
	120	0.2	0.2	0.3	10.844
	150	0.0	0.2	0.5	11.340
	200	0.1	-0.1	0.0	12.011
0.3	40	0.0	0.5	0.9	8.122
	80	0.1	0.3	0.4	10.000
	120	0.1	0.4	0.4	11.293
	150	0.0	0.4	0.4	12.075
	200	-0.1	-0.1	-0.1	13.163

Table 6 Results of error analysis ($D = 70$ mm, $F_h = 100$ m).

Shear exponent: α	Height (m)	Δ_C (%)	Δ_S (%)	Δ_H (%)	U_t (m/s)
0.0	40	0.0	-0.1	0.0	10.000
	80	0.1	0.0	0.1	10.000
	120	-0.1	-0.1	0.0	10.000
	150	0.1	-0.1	-0.1	10.000
	200	0.1	-0.1	-0.2	10.000
0.1	40	-0.2	0.2	0.4	9.330
	80	0.1	0.8	0.7	10.000
	120	0.1	-0.6	-0.6	10.414
	150	0.0	-0.1	0.0	10.649
	200	-0.1	-0.2	-0.2	10.960
0.2	40	0.0	0.5	1.0	8.706
	80	-0.1	1.6	1.6	10.000
	120	0.0	-0.8	-1.0	10.844
	150	-0.1	-0.2	-0.1	11.340
	200	0.0	-0.1	-0.2	12.011
0.3	40	0.2	1.0	1.6	8.122
	80	0.1	2.3	2.4	10.000
	120	-0.1	-1.2	-1.3	11.293
	150	0.2	-0.3	-0.2	12.075
	200	-0.1	0.0	0.0	13.163

error values in the tables tend to become larger for lower heights, since the true wind speeds have smaller values for lower heights (see, eq. (9) and the values of U_t in tables 3 to 6). The NORSEWInD standard stated the acceptance criteria of lidar performance for wind resource assessments, and the acceptance criteria for a linear regression slope between 0.98 and 1.01 has been stated[14]. This corresponds to -2% to $+1\%$ error, and these values are references for investigation on the values in the tables. Basically, the error becomes larger when the change of wind speed or the SNR weighting are steep and asymmetric. To clarify this tendency, representative values in the tables are plotted in Figs. 8 to 10. Figure 8 shows the comparison of height profiles of the three errors (caused by shear curvature, SNR weighting, and height sensing error) in the case of the receiving aperture diameter of 0.04 m and the beam focusing height of 100 m. The error caused by shear curvature is not so distinct compared with other error sources, but the error considering SNR weighting and height sensing error are more than $+1\%$ around the beam focusing height because of the steep change of

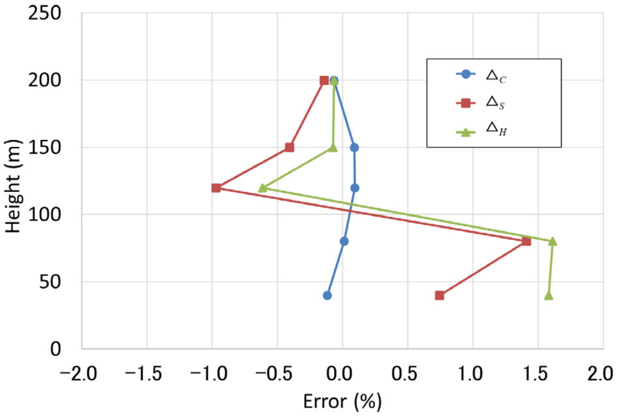

Fig. 8 Height profile of each error ($D = 0.04$ m, $F_h = 100$ m, $\alpha = 0.3$).

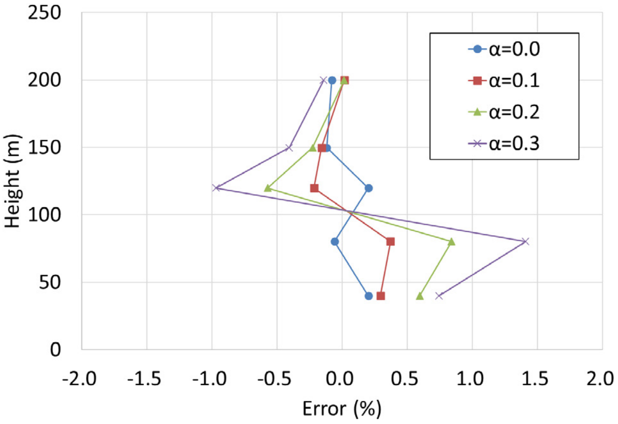

Fig. 9 Height profile of error caused by SNR weighting (Δ_S) for each shear exponent ($D = 0.04$ m, $F_h = 100$ m).

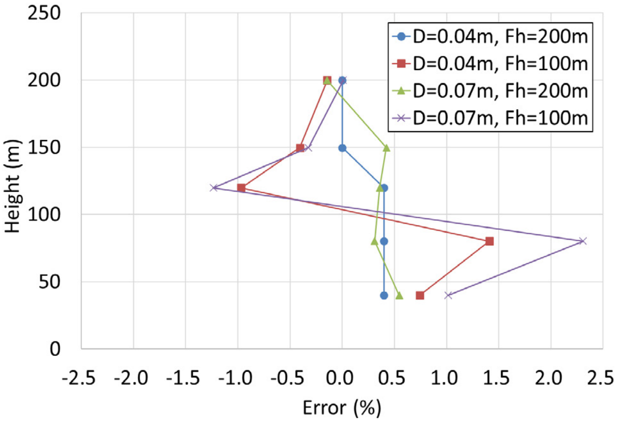

Fig. 10 Height profile of error caused by SNR weighting (Δ_S) for each condition of receiving aperture diameter and focal height ($\alpha = 0.3$).

weighting at the region. It is known that the SNR weighting and heigh sensing error should be taken care of in wind resource assessment. Figure 9 shows the height profile of error Δ_S (caused by SNR weighting) for each shear exponent for the case of same value of the receiving aperture diameter and the beam focusing height in Fig. 8. The error becomes larger for the larger values of shear exponent α and exceeds $+1\%$ in the case of $\alpha = 0.3$ which is a realistic shear flow at the field for wind energy[18]. Figure 10 shows height profile of Δ_S regarding each condition of the receiving aperture diameter and the beam focusing height in the case of the above-mentioned realistic shear flow (i.e., $\alpha = 0.3$). The larger receiving aperture diameter and the lower beam focusing height realize the higher SNR at the beam focusing height (see, Fig. 7(c)). The higher SNR contributes to high data availability which is outside the scope of this paper but important term in wind resource assessment[9]. However, the above-mentioned situations (larger receiving aperture diameter and/or lower beam focusing height) cause steeper change and stronger asymmetry on SNR weighting around the beam focusing height (see eq. (8) and Fig. 7(c)). Therefore, the error Δ_S caused by SNR weighting and Δ_H caused by height sensing error become larger for these cases. Totally, the error is determined quantitively by the combination of the above-mentioned tendencies. Parameters of VAD-PCDL (especially, the receiving aperture diameter and the beam focusing height) should be optimized by considering requirements regarding wind speed measurement accuracy and data availability in wind resource assessment. This optimization can be realized by understanding the error sources (Δ_C, Δ_S, and Δ_H) quantitively and independently. For example, if Δ_S is the dominant factor in the error, the beam focusing effect should be reduced by tuning the receiving aperture diameter or the beam focusing height. If, only Δ_H is dominant, the sampling interval of A/D converter should be shorter. If Δ_C is dominant, this means the error source is the wind field itself. In such a case, making pulse width shorter for higher range resolution might be effective. This reduces the volume averaging effect along with LOS direction, even though the shorter pulse causes spectral broadening and negative influence on the accuracy of wind speed measurement. This influence should be paid attention.

In the tables, the three errors become small and theoretically should be zero for the cases of $\alpha = 0$, since wind speed uniformly distributes in this case. There are contradictions with the values lower than or equal to 0.2% which do not correspond to the above-mentioned theory. The error of 0.2% is not negligible by considering the acceptance criteria (wind speed measurement accuracy of 1%) in wind resource assessment[14]. The reason of the contradictions should be investigated further, but this may be caused by the limited iteration number of the Monte-Carlo simulation (i.e., 16,000) or the thickness of sliced atmosphere. Also, there is a possibility that the signal processing algorithm (i.e. FFT-based, here) is the source of this irregularities. The interval of Doppler velocity bin in the spectrum, which is determined by the wavelength, sampling interval, and the sample number in the range gate, is 4.84 m/s. On the other hand, the wind speed at the reference height of 80 m is 10 m/s, and the error corresponding to 0.2% error is 0.02 m/s (see Fig. 11). This error corresponds to the 1/242 (very small) of the velocity bin interval. Therefore, it is not easy to realize this velocity estimation accuracy, even though the spectral moment estimation of eq. (1) could realize the accurate estimation with 0.2% as shown in tables 3-6. Some additional processing (for example, zero-padding[27]) has potential to reduce the error. However, the simple FFT-based method has been employed here since this method has an advantage regarding the real-time processing. The effect of the above-mentioned additional processing can be simulated easily by adopting the processing to the simulated heterodyne-detected signals.

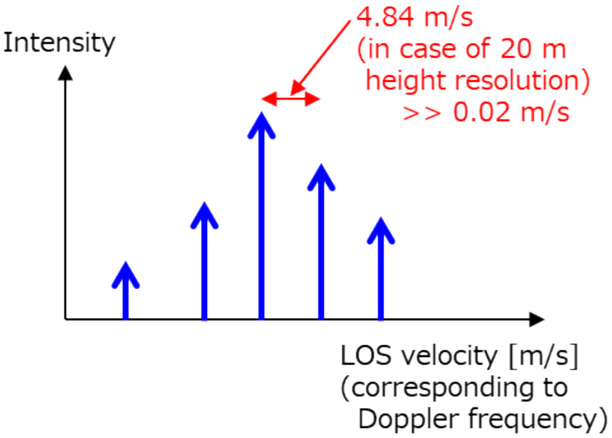

Fig. 11 Schematic of velocity bin of spectrum.

8. Comparison with past works

Here, the simulation procedure of this paper is compared with the past work which investigated the error in shear flow. The comparison is summarized in Table 7. While the procedure in the past works18, 19) has used simplified numerical integration, this paper has employed the full Monte-Carlo simulation. Pulse shape is the only PCDL parameter which has been considered in the past works18, 19). This means the error which has been investigated in the past works18, 19) was only Δ_C. The influences of SNR profile and A/D conversion have been considered only in this paper. Consideration of these factors can be possible also for the past works18, 19) by modifying the equation. However, the influences of the speckle noise, detector noise, spectral accumulation, and estimation algorithm can be considered exactly only in this paper. The weak point for the procedure of this paper is the time consumption. The simplified method of the past works18, 19) is suitable to know rough tendency of influences regarding shear condition and PCDL performance.

Table 7 Comparison between simplified numerical integration and full Monte-Carlo simulation.
(○ : considered, × : not considered)

Terms		Simplified numerical integration (eqs. (9) and (10) in [18], eq. (4) in [19])	Full Monte-Carlo simulation (this paper)
PCDL performance	Pulse shape	○[*1]	○
	SNR profile	×[*2]	○
	Speckle noise	×	○
	Detector noise	×	○
	A/D conversion	×[*2]	○
	Spectral accumulation	×	○
	Estimation algorithm	×	○
Calculation time		Short	Time consuming

*1 Triangle pulse shape has been employed in eq. (10) in [18] but can be replaces by more realistic shape.

*2 These factors can be considered in eq. (9) in [18] by using convolution and discretization which correspond to consideration of SNR and digitization.

9. Conclusions

Full-parameter performance simulation theory was shown for VAD-PCDL. Example analysis of wind speed measurement error is shown for the case of sheared wind flow. Some cases of the vertical wind profiles with shear were set for the input, and wind speed measurements using VAD scan were simulated using the FFT based signal processing. The larger receiving aperture diameter and the lower beam focusing height realize higher SNR at the beam focusing height and contributes to high data availability. However, these situations caused steeper SNR weighting around the beam focusing height. The errors caused by SNR weighting and/or height sensing error became larger for these cases while the shear curvature was not so distinct compared with other error sources. The errors regarding SNR weighting and height sensing error were more than +1% in some cases, and this error cannot be ignored in wind resource assessments if the NORSEWInD standard is referred. The simulation theory and results of this paper can clarify the source of errors in VAD-PCDL measurement. This clarification contributes to the optimized parameter design of VAD-PCDL (especially, the receiving aperture diameter and the beam focusing height), by considering requirements regarding horizontal wind speed measurement accuracy and data availability in wind resource assessment for wind energy application.

Although the wind field of this paper is limited in a simple case (i.e., horizontal shear with power law), the above-mentioned tendency on measurement error can be the basis of understanding for general wind field cases. The detector noise was neglected in the concrete simulation. However, this influence can be considered simply by using the noise term in eq. (5). Although the simulation in this study is limited for the case of a flat terrain, this can be modified for the measurement in a complex terrain by using the complex wind flow as an input. The application to the floating

VAD-PCDL systems for the offshore wind resource assessment is also possible, by combining with the motion of the buoy and the motion compensation algorithm. The scope of this paper has been limited in pulsed CDLs even though continuous-waves CDLs (CCDLs) have been also used in wind resource assessments10, 11, 14). Ranging in a CCDL is performed by utilizing the beam focusing effect, therefore, error caused by SNR weighting should be considered more carefully.

Acknowledgement

A part of this study was performed in the activity of the IEA WIND Task 32 Work-Package 1 in 2014. The author thanks the Task 32 for giving the opportunity to perform this study.

References

1) R. M. Huffaker and R. M. Hardesty, "Remote sensing of atmospheric wind velocities using solid-state and CO2 coherent laser systems," Proc. IEEE, **84**(2), 181–204 (1996).
2) J. M. Vaughan, K. O. Steinvall, C. Werner, and P. H. Flamant, "Coherent laser radar in Europe," Proc. IEEE, **84**(2), 205–226 (1996).
3) C. J. Karlsson, F. Å. A. Olsson, D. Letalick, and M. Harris, "All-fiber multifunction continuous wave coherent laser radar at 1.55 μm for range, speed, vibration, and wind measurement," Applied Optics, **39**(21), 3716–3726 (2000).
4) G. N. Pearson, R. J. Roberts, J. R. Eacock, and M. Harris, "Analysis of the performance of a coherent pulsed fiber lidar for aerosol backscatter applications," Applied Optics, **41**(30), 6442–6450 (2002).
5) J. P. Cariou, B. Augere, and M. Valla, "Laser source requirements for coherent lidars based on fiber technology," Comptes Rendus Physique, **7**(2), 213–223 (2006).
6) S. Kameyama, T. Ando, K. Asaka, Y. Hirano, and S. Wadaka, "Compact all-fiber pulsed coherent Doppler lidar system for wind sensing," Applied Optics, **46**(11), 1953–1962 (2007).
7) T. Ando, S. Kameyama, and Y. Hirano, "All-fiber coherent Doppler lidar technologies at Mitsubishi Electric Corporation," IOP Conference Series: Earth and Environmental Science, **1**, 012011 (2008).
8) M. Courtney, R. Wagner, and P. Lindelöw, "Testing and comparison of lidars for profile and turbulence measurements in wind energy," IOP Conference Series: Earth and Environmental Science, **1**, 012021 (2008).
9) N. Kotake, H. Sakamaki, M. Imaki, Y. Miwa, T. Ando, Y. Yabugaki, M. Enjo, and S. Kameyama, "Intelligent and compact coherent Doppler lidar with fiber-based configuration for robust wind sensing in various atmospheric and environmental conditions," Optics Express, **30**(11), 20038–20062 (2022).
10) D. A. Smith, M. Harris, A. S. Coffey, T. Mikkelsen, H. E. Jørgensen, J. Mann, and R. Danielian, "Wind lidar evaluation at the Danish wind test site in Høvsøre," Wind Energy, **9**(1–2), 87–93 (2006).
11) C. B. Hasager, A. Peña, M. B. Christiansen, P. Astrup, M. Nielsen, F. Monaldo, D. Thompson, and P. Nielsen, "Remote sensing observation used in offshore wind energy," IEEE Journal of Selected Topics in Applied Earth Observations and Remote Sensing, **1**(1), 67–79 (2008).
12) A. Clifton, P. Clive, J. Gottschall, D. Schlipf, E. Simley, L. Simmons, D. Stein, D. Trabucchi, N. Vasiljevic, and I. Würth, "IEA Wind Task 32: Wind lidar identifying and mitigating barriers to the adoption of wind lidar," Remote Sensing, **10**(3), 406 (2018).
13) J. Gottschall, B. Gribben, D. Stein, and I. Würth, "Floating lidar as an advanced offshore wind speed measurement technique: current technology status and gap analysis in regard to full maturity," Wiley Interdisciplinary Reviews: Energy and Environment, **6**(5), e250 (2017).
14) C. B. Hasager, D. Stein, M. Courtney, A. Peña, T. Mikkelsen, M. Stickland, and A. Oldroyd, "Hub height ocean winds over the North Sea observed by the NORSEWInD lidar array: measuring techniques, quality control and data management," Remote Sensing, **5**(9), 4280–4303 (2013).
15) S. Nabi, N. Nishio, P. Grover, R. Matai, Y. Kajiyama, N. Kotake, S. Kameyama, W. Yoshiki, and M. Iida, "Improving LiDAR performance in complex terrain using CFD-based correction and direct-adjoint-loop optimization," Journal of Physics Conference Series, **1452**(1), 012082 (2020).
16) IEA WIND Recommended Practices 15, "Ground-based vertically-profiling remote sensing for wind resource assessment," First Edition, (2013).
17) IEA WIND Recommended Practices 18, "Floating lidar systems," First Edition, (2017).
18) M. Courtney, A. Sathe, and N. G. Nygaard, "Shear and turbulence effects on lidar measurements," DTU Wind Energy, (E-0061), (2004).
19) J. K. Lundquist, M. J. Churchfield, S. Lee, and A. Clifton, "Quantifying error of lidar and sodar Doppler beam swinging mea-

surements of wind turbine wakes using computational fluid dynamics," Atmospheric Measurement Techniques, **8**(2), 907–920 (2015).

20) D. Zrnic, "Estimation of spectral moments for weather echoes," IEEE Transactions on Geoscience Electronics, **GE-17**(4), 113–128 (1979).
21) R. Frehlich, "Effects of wind turbulence on coherent Doppler lidar performance," Journal of Atmospheric and Oceanic Technology, **14**(1), 54–75 (1997).
22) S. Kameyama, T. Ando, K. Asaka, Y. Hirano, and S. Wadaka, "Performance of discrete-Fourier-transform-based velocity estimators for a wind-sensing coherent Doppler lidar system in the Kolmogorov turbulence regime," IEEE Transactions on Geoscience and Remote Sensing, **47**(10), 3560–3569 (2009).
23) R. G. Frehlich and M. J. Kavaya, "Coherent laser radar performance for general atmospheric refractive turbulence," Applied Optics, **30**(36), 5325–5352 (1991).
24) S. Kameyama, T. Ando, K. Asaka, and Y. Hirano, "Semianalytic pulsed coherent laser radar equation for coaxial and aperture systems using nearest Gaussian approximation," Applied Optics, **49**(27), 5169–5174 (2010).
25) R. Wagner, M. Courtney, J. Gottschall, and M. P. Lindelöw, "Accounting for the speed shear in wind turbine power performance measurement," Wind Energy, **14**(8), 993–1004 (2011).
26) R. Wagner, I. Antoniou, S. M. Pedersen, M. S. Courtney, and H. E. Jørgensen, "The influence of the wind speed profile on wind turbine performance measurements," Wind Energy, **12**(4), 348–362 (2009).
27) L. Fan, G. Qi, J. Xing, J. Jin, J. Liu, and Z. Wang, "Accurate frequency estimator of sinusoid based on interpolation of FFT and DTFT," IEEE Access, **8**, 44373–44380 (2020).

Author introduction

Shumpei Kameyama received his M.E. degree from Keio University in 1995 and D.E. degree from Chiba University in 2011. Since 1995, he has been with Mitsubishi Electric Corporation, and he started the development of laser remote sensing systems in 1999. His current research involves coherent Doppler lidar, differential absorption lidar, and range imaging laser sensor. He is a member of IEEE, Optica, Japan Society of Applied Physics, and Laser Radar Society of Japan. He has received Technology Award from Japan Society for Aeronautical and Space Science, Technology Management Innovation Award from Japan Techno-Economics Society, and Significant Contributor Award from RTCA. He has elevated to IEEE Fellow in 2024.

LRSJ Laser Radar Society of Japan レーザセンシング学会
レーザセンシング学会誌　第5巻第1号(2024)

第41回レーザセンシングシンポジウム開催報告

酒井　哲[1]，染川 智弘[2]，吉田　智[1]，西橋 政秀[1]，
及川 栄治[1]，永井 智広[1]，瀬古　弘[1]
（[1] 気象研究所, [2] レーザー技術総合研究所）

（Received November 30, 2023）

2023年9月6日から8日にかけて茨城県つくば市にある文部科学省研究交流センターにおいて，第41回レーザセンシングシンポジウム（LSS41）が開催された．開催形式は，口頭発表と基礎セミナーが現地・オンラインのハイブリッド形式，ポスター発表は現地のみであった．参加人数は現地参加者が92名，オンライン参加者が10名であった（うち学生14名）．前回の参加者数（現地59名，オンライン32名）と比べると現地参加者数の割合が大きく増えた．これは新型コロナウイルス感染症対策による行動制限が緩和された影響が大きい．また，現地での対面形式を望む人が多かったことがうかがえる．なお，協賛企業は17社で，その中から12件の企業展示があった．発表件数は，口頭（特別講演を含む）が32件（うち学生3件），ポスター22件（うち学生7件）であった．前回シンポジウムと比較すると，口頭発表が5件増え，ポスター発表は同件数であった．当日の天気は1日目と2日目は曇りまたは雨となり，前日まで続いていた猛暑は若干おさまった．3日目は台風13号の接近により午前中は大雨となったが，午後には雨域が通り過ぎ，予定通りシンポジウムを行うことができた．

写真-1　シンポジウム会場（文部科学省研究交流センター）

1日目（9月6日（水））

13時からLSS基礎セミナーが行われた．講師は柴田泰邦先生（東京都立大学）と青木誠先生（情報通信研究機構）が担当し，内容は柴田先生が「各種大気ライダーの送信系・受信系の基礎」，青木先生が「レーザセンシングで使われるレーザの基礎」であった．2件の講演ともにレーザセンシングの基礎について，ご自身の研究経験に基づいて説明され，初心者にとっても分かりやすく有益な内容であった．質疑ではレイリーライダーの気温測定精度，今後ライダーで測ってみたい物質，DIALの気温測定原理，半導体レーザの高出力化，固体パルスレーザーの高繰り返し等について質問があった．なお，これら講演の録画資料がLSS41参加者限定ページに公開されている（https://laser-sensing.jp/lss41/papers/LSS41BasicSeminar.html）.

2日目（9月7日（木））

2日目は9時から開会式が行われ，実行委員長と長澤会長による開会の挨拶があった．続いて松村崇行気象研究所長から来賓挨拶があり，レーザセンシングへの今後の期待が述べられた．午前中は2つの口頭発表セッションが行われた．前半のセッション（ライダー観測・データ利用）では，ライダーによる海外（南極点，フィリピン，モンゴル），国内（立川，九州）での観測結果について発表があった．観測対象は氷雲，降水・降雪，黄砂ダスト，水蒸気，超高層大気中のカルシウム原子・イオンと多岐に渡っていた．後半のセッション（飛翔体搭載ライダー）では，衛星搭載ライダーによるエアロゾル組成の解析，衛星搭載風ライダーのシミュレーション，国際宇宙ステーション搭載植生ライダー（MOLI）の進捗状況，光無線給電のための差分吸収画像を用いた太陽電池位置の検出方法について発表があった．

写真-2　口頭発表の様子

ポスターセッションは企業展示と同じ会場で行われた．計22件の発表があり，コーヒー，紅茶などを飲みながら研究成果について活発な議論が行われていた．また同時に，企業展示ブースでは製品等についての情報交換が活発に行われていた．

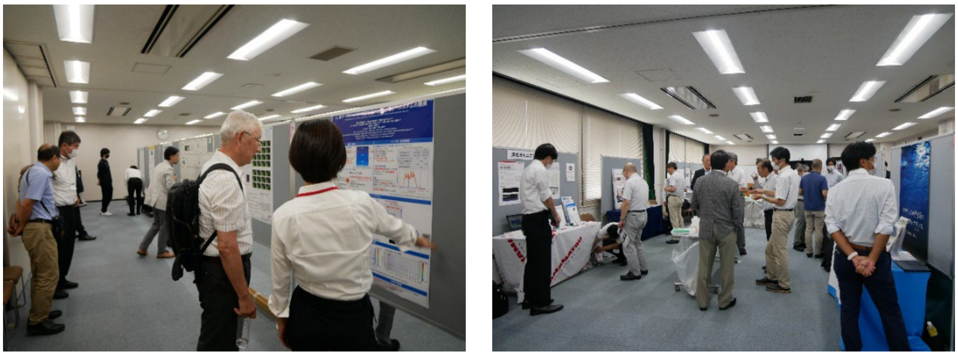

写真-3　ポスターセッションの様子（左），企業展示の様子（右）

特別講演では，テーマを「防災分野におけるレーザセンシング技術の利用」として，清水慎吾先生（防災科学技術研究所），田中昌之先生（気象研究所）による講演があった．清水先生からは，「極端気象予測の精度向上にむけた最新観測・予測研究の紹介」というタイトルで，毎年のように多発する線状降水帯に対して，避難に必要な猶予時間（リードタイム）が確保できる時刻までに正確な雨量予測を行うことを目的として実施された，水蒸気ライダーや風ライダー，地上デジタル波，マイクロ波放射計等の最新の観測技術の開

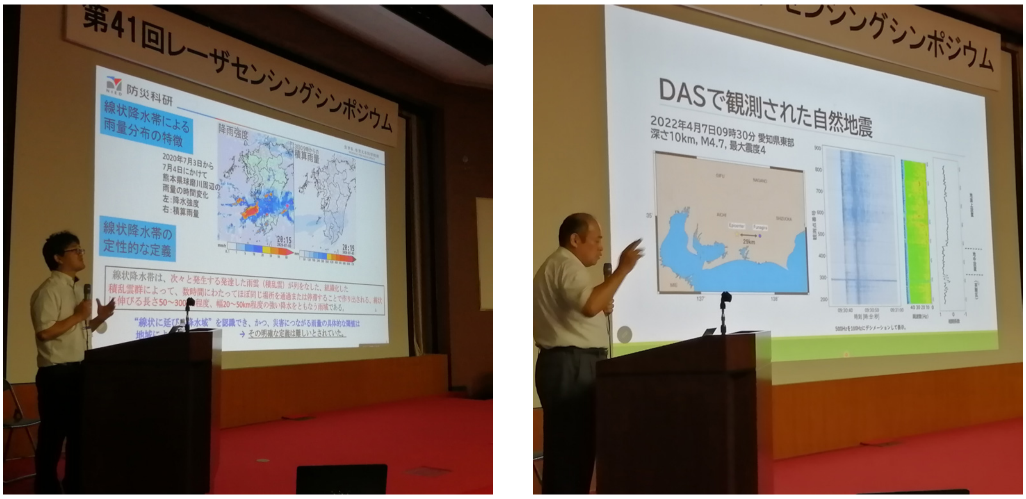

写真-4　特別講演（左：清水慎吾先生，右：田中昌之先生）

発と，最新の数値予測システムを用いた予測結果が報告された．これらの成果から，半日前から2時間前程度のリードタイムを確保でき，自治体の避難区分単位で避難が必要なエリアを絞り込むことで「逃げ遅れ」被害の軽減に貢献できるとのことであった．田中先生からは，「光ファイバセンサの発展と地震観測への活用」というタイトルで講演があった．光ファイバセンサの原理は，光ファイバにレーザ光を入射し，光ファイバのわずかな不均一性により後方散乱された光を検出することで，光ファイバ経路にそったひずみや温度の分布を測定するものである（有線のライダーとも言える）．地震計を設置することが難しい海底や火山周辺に光ファイバケーブルを設置すれば，地震を線状に観測できるため，海底を震源とする地震の多い日本では，有効な観測手段として期待されているとのことであった．

懇親会は17:30からつくば駅近くのBeer & Cafe Engiで行われた．参加者数は58名で，ビールやワイン，ソフトドリンクと食事を楽しみながら，久しぶりに対面で親睦を深めることができた．一方で，マイクの音が聞きづらかったという意見もあった．

写真-5　懇親会の様子

3日目（9月8日（金））

3日目は小林喬郎先生（レーザセンシング学会理事・名誉会員）の訃報の知らせが長澤会長から伝えられたため，口頭発表セッション開始前に小林喬郎先生のご冥福を祈り，参加者全員で1分間の黙とうを捧げた．その後午前中から午後にかけて3つの口頭発表セッション（ライダー技術・レーザ技術，ライダー技術・レーザセンシングI，II）が行われた．ライダー技術・レーザ技術のセッションでは，エアロゾル，気温，水蒸気，風などのライダーとしてはオーソドックスな測定対象を，新しい技術を使って測定する技術開発成果について発表があった．ライダー技術・レーザセンシングIのセッションでは，アンモニア，微生物，爆発物，トンネルの浮石，水中の油を遠隔計測する研究成果について発表があった．ライダー技術・レーザセンシングIIのセッションでは，ライダーとシミュレーションによる二酸化炭素の排出源推定，CRDS（Cavity Ring Down Spectroscopy）技術を用いた高感度微量ガス濃度計測技術の開発，LIBS（Laser Induced Breakdown Spectroscopy）技術を用いた磁器がいし汚染度計測，地上-衛星間レーザ長光路吸収による大気微量ガス測定について発表があった．

最後に授賞・閉会式が行われた．今回のレーザセンシング学会若手奨励賞（廣野賞）の受賞者は橋本彩香氏（電気通信大学，M2）で，発表タイトル「超高層大気中に分布する金属原子・イオンの共鳴散乱ライダー全夜観測」が表彰された．橋本氏をはじめ，学生の皆様の今後のご活躍に期待したい．また，2022年度レーザセンシング学会論文賞の記念品贈呈も同時に行われた．受賞論文は「工場内浮遊粒子状物質の測定を目的とする小型ミー散乱ライダーの開発」，著者は左成信之氏，板谷庸平氏，横川守久氏（柴田科学），神慶孝氏，杉本伸夫氏，西澤智明氏（国立環境研究所）であった．

来年度のレーザセンシングシンポジウムは，大阪で予定されている（実行委員長は染川智弘氏）．今後のシンポジウムでは，新規分野からの参入，若い研究者の参加が増えることを期待する．

写真-6　授賞式（上：廣野賞，下：レーザセンシング学会論文賞）

謝辞：開催準備に当たりレーザセンシング学会企画委員会の藤井隆氏，江尻省氏，今城勝治氏から数々の有益なご助言を頂いた．ホームページ作成・管理においては杉本伸夫氏，清水厚氏にご協力頂いた．学生アルバイトの方々にはシンポジウム受付や照明，タイムキーパーとしてご協力頂いた．ここに感謝する．

写真-7　集合写真

LRSJ Laser Radar Society of Japan レーザセンシング学会

レーザセンシング学会誌　第 5 巻第 1 号（2024）

AGU Fall Meeting 2023 参加報告

ラゴロサス ノフェル（Nofel Lagrosas）

（九州大学）

（Received January 29, 2024）

2023 年 12 月 11 日から 15 日まで，米国サンフランシスコのモスコーニセンターで 2023 年米国地球物理学連合（American Geophysical Union: AGU）秋季大会が開催された．会議には 2 万人以上の直接参加者があった．口頭セッションは，昨年同様にオンサイト（対面）とオンラインのハイブリッド開催となった．口頭発表は，ライブストリーミングされ，セッション終了後 72 時間まで AGU イベントアプリまたはオンラインプラットフォームで視聴できた．また，それらの動画は，2024 年 3 月までオンデマンドで視聴することができる．さらに，今年の会議には新しい機能が追加された．現地開催期間とは別に設けられた 2024 年 1 月 22 日から 25 日にかけてのオンライン・ポスター発表である．これは，直接参加しないことを選択した人々のためのものである．

今年の秋季大会では，大気科学部門の幅広いトピックが発表された．その中には，大気力学，大気質，近年頻発している熱波や豪雨の分析などの気象・気候研究に関する最新の研究が含まれている．また，エアロゾル，雲，大気微量成分，気象要素を精測する先端的な直接計測およびリモートセンシング手法や，大気組成等を定量化するためのデータ駆動型手法などの新しい解析手法についての発表があった．AGU では膨大な数のトピックが発表されるため，自分の研究が他の分野とリンクする可能性は常に高い．この会議に直接参加することは，他の研究者と協力し，国際的な共同研究に携わるチャンスである．この会議で報告された共同研究活動はいくつかある．これらの共同研究の現状が報告されている．NASA の Gregory Schuster が主導する MIRA（Models, In situ, and Remote sensing of Aerosols）プロジェクトや，リール大学の Oleg Dubovik が主導する GRASP（Generalized Retrieval of Aerosol and Surface Properties）プロジェクトやネットワークなどである．今回の会議では，著者は夜間雲観測の現在の進展についても発表した．これは夜間の雲を検出・分析するための共同観測である．また，リモートセンシングによる雲観測と測定に関するセッションも行った．

エアロゾルに関する現在の研究キャンペーンの結果が報告されている．そのひとつが，現在バルバドスを拠点とする海軍研究所の MAGPIE（Moisture and Aerosol Gradients/Physics of Inversion Evolution）プロジェクトである．ウィスコンシン大学ライダーチームの Edwin Eloranta らは，高分解能ライダー（HSRL）を使ってバルバドスの境界層でサハラ砂漠のダストをモニターした結果を発表した．現在のライダー技術開発も報告された．アプトンにあるブルックヘブン国立研究所の Fan Yang らは，サブメーター分解能で大気雲を観測するための，時間ゲート，時間相関単一光子計数ライダーの開発に関する成果を報告した．その結果，～10 cm の空間分解能で雲の光学パラメータを検出し定量化できる可能性が示された．このライダーシステムの開発は，将来，雲の内部構造や大気中のエアロゾルと雲の相互作用のより詳細な理解への道を開くことができる．

次回の AGU 秋季総会は，2024 年 12 月 9～13 日にワシントン D.C. で開催される．

学会誌への投稿案内

レーザセンシング学会誌では，レーザセンシングに関する研究・技術や最新の研究成果に関する，「論文」,「総説（レビュー）」,「小論文（レター）」，および「解説」記事を，会員・非会員を問わず随時応募しています．投稿に関する手続きや要件については，学会ホームページをご参照ください．学会誌は，これまで年2回（4月および10月）の発刊を行ってまいりましたが，今後は年1回の発刊に変更致します．ご不便をおかけ致しますが，皆様の投稿を引き続きお待ちしております．

学会ホームページ
https://laser-sensing.jp/

学会誌ホームページ
https://laser-sensing.jp/gakkaishi.html
＊最新版の投稿規定，執筆要領，テンプレート，および投稿フォームは，画面上部のリンクからダウンロードいただけます．

「学位論文紹介」投稿のお願い

レーザセンシング学会誌では，学会員が発表した博士論文および修士論文の紹介を行っています．下記の要領に従って投稿をお願いいたします．

1. 掲載条件

2021年4月1日から2024年3月31日の間に授与された博士および修士の学位に対する学位論文を対象とします．博士論文は題目リストおよび要旨を，修士論文は題目リストのみを掲載します．

2. 投稿方法

下記の情報をレーザセンシング学会編集委員会（lrsj-edit_office@laser-sensing.jp）へお送りください．様式は任意です．

（1）大学院，研究科，専攻の名称
（2）取得学位，学位取得年月
（3）著者名
（4）論文題目
※博士論文の場合は，下記（5）～（7）もご提出ください．
（5）キーワード（4～5ワード）
（6）要旨（1500字以内．図表掲載可．）
※図表に対応する文字カウント数は，標準的な大きさ，縦横比の図の場合で400字/個程度となる．
（7）顔写真（任意）

3. 投稿期限

2024年6月10日

4. その他

掲載料は無料です．

正誤表

レーザセンシング学会誌3巻2号（2022年10月発行），レーザセンシング学会ニュースレター10号（2023年1月発行）において，掲載内容に誤りがございました．

お詫び申し上げますとともに，下記のとおり訂正させていただきます．

レーザセンシング学会誌3巻2号 66–67ページ，巻頭言「産業応用ライダー特集：緒言」小林喬郎著

修正箇所	誤	正
66ページ21行目	国立環境研究研，竹内延夫グループ：大型ライダーよる東アジア域大気計測	国立環境研究研，杉本伸夫グループ：ライダーネットワークによる東アジア域大気計測
67ページ4行目	3）O. Uchino, M. Maeda, J. Konno, T. Shibata, C. Nagasawa, and M. Hirono, “Observation of strastspheric ozone by a XeCl	3）O. Uchino, M. Maeda, J. Konno, T. Shibata, C. Nagasawa, and M. Hirono, “Observation of stratospheric ozone by a XeCl
67ページ6行目	4）O. Uchino, M. Maeda, and Y. Miyazoe, “Differential-absorption lidar measurement of ozone with excimer- Raman hybrid	4）O. Uchino, M. Maeda, and Y. Miyazoe, “Differential-absorption lidar measurement of tropospheric ozone with excimer- Raman hybrid
67ページ8行目	5）H. Shimizu, Y. Sasano, H. Nakano, N. Sugimoto, I. Matsui, and N. Takeuchi, “Large scale laser radar for measuring aerosol	5）H. Shimizu, Y. Sasano, H. Nakane, N. Sugimoto, I. Matsui, and N. Takeuchi, “Large scale laser radar for measuring aerosol
67ページ16行目	9）平野嘉仁，“巻頭言　ライダー技術と産業応用，”レーザセンシング学会誌．**2**, 1–3（2021）．	9）平野嘉仁，“巻頭言　ライダー技術の発展と産業応用，”レーザセンシング学会誌．**2**, 1–3（2021）．
67ページ18行目	11）国内特許，丹野直弘，市村勉，佐伯昭雄，“光波反射像測定装置，”2010042号（1990）．	11）国内特許，丹野直弘，市村勉，佐伯昭雄，“光波反射像測定装置，”特開平4–173245（1990）．

レーザセンシング学会ニュースレター10号 2–5ページ，「第40回レーザセンシングシンポジウム　開催報告」香川直己，酒井哲著

該当箇所	誤	正
4ページ 右段 11行目	今回のシンポジウムの参加者数は，主会場で現地66	今回のシンポジウムの参加者数は，主会場で現地59
4ページ 右段 12行目	名とオンライン29名の併せて95名，セミナー会場で23	名とオンライン32名の併せて91名，セミナー会場で23

編集後記

前号からニュース記事も学会誌に採録しております．今号では，2編の英語論文，2本のニュースを採録しました．巻頭言は，気象庁と大学でライダーを用いた大気研究をなさってきた名古屋大学の甲斐先生にご執筆いただきました．論文は成層圏エアロゾルのライダー観測，ドップラーライダーによる風観測のシミュレーション，ニュースはレーザセンシングシンポジウム開催報告と海外の学会参加報告となっており，充実した内容になっております．

次号から発刊回数が年2回から年1回に変更となります．会員のみなさまへの情報提供の機会の喪失につながらぬよう，学会誌の内容の拡充を推し進めて参りますので，今後とも変わらぬご愛顧賜りますよう，どうぞよろしくお願い申し上げます．

編集委員会　委員　及川　栄治

■編集兼発行人：レーザセンシング学会（http://laser-sensing.jp/）

■連絡先：〒305-0052 茨城県つくば市長峰1-1　気象庁気象研究所　気象観測研究部
第2研究室気付　レーザセンシング学会編集委員会
■電子メール：lrsj-edit_office@laser-sensing